SIAM J. Applied Dynamical Systems
Vol. 19, No. 3, pp. 1701–1735


# Big Ducks in the Heart: Canard Analysis Can Explain Large Early Afterdepolarizations in Cardiomyocytes*

Joshua Kimrey†, Theodore Vo‡, and Richard Bertram§

**Abstract.** Early afterdepolarizations (EADs) are pathological voltage fluctuations that can occur in cardiac cells and are a potent source of potentially fatal arrhythmias. Recent works examining the mechanisms underlying EADs in minimal computational cardiac models have revealed that voltage-driven EADs are canard-induced mixed-mode oscillations whose properties are mediated by the rate at which these cells are paced. In this work, we analyze the mechanisms for the pacing-induced generation of different EAD behaviors in a reduced four-dimensional Luo–Rudy I model using slow-fast analysis. While previous explanations for EADs in this model have required manipulation of the underlying multitimescale structure, our approach does not and we find that the canard mechanism persists in generating EADs in this context. We also find that the canard mechanism gives a more complete explanation for the onset and properties of the EADs induced (e.g., EAD amplitude and number). In addition, we also find that the canards play an essential role in producing a richer set of behaviors than were seen in other minimal models, some of which have also been observed in experiments. These behaviors include pacing-induced termination of EADs, the periodic alternation of cardiac action potentials with and without EADs, as well as bistability between standard and EAD-containing action potentials at a fixed pacing rate. Finally, we show that this bistability can lead to hysteretic transitions between standard and arrhythmogenic action potentials under sufficiently slow oscillations in the pacing rate.

**Key words.** excitable media, early afterdepolarizations, mixed-mode oscillations, canards, cardiac

**AMS subject classifications.** 37B55, 92B25

**DOI.** 10.1137/19M1300777

## 1. Introduction.

Early afterdepolarizations (EADs) are pathological voltage fluctuations that can occur in cardiac action potentials (APs). As a result of these fluctuations, the APs are prolonged (compare Figures 1(a) and 1(b)), which can lead to arrhythmias in cardiac tissue [11, 26, 44, 48]. The EADs can be induced in isolated cardiac muscle cells (cardiomyocytes) by putting the cells into a hypokalemic (low $K^+$) solution [25, 30, 31, 49], and can also be observed following the application of drugs that act on $K^+$, $Na^+$, or $Ca^{2+}$ on channels [2, 4, 17, 37, 38].

Several mathematical studies have been performed aimed at understanding the dynamical basis of EADs [22, 23, 24, 34, 35, 36, 43, 45, 52]. Recent studies have employed slow-fast analysis, also known as geometric singular perturbation analysis, to facilitate this understand-

*Received by the editors November 19, 2019; accepted for publication (in revised form) by J. Sneyd April 29, 2020; published electronically July 22, 2020.
https://doi.org/10.1137/19M1300777
**Funding:** The work of the second and third authors was funded by the National Science Foundation, DMS-1853342.
†Department of Mathematics, Florida State University, Tallahassee, FL 32306 (jkimrey@math.fsu.edu).
‡School of Mathematics, Monash University, Melbourne, Australia (theodore.vo@monash.edu).
§Department of Mathematics, and Programs in Neuroscience and Biophysics, Florida State University, Tallahassee, FL 32306 (bertram@math.fsu.edu).

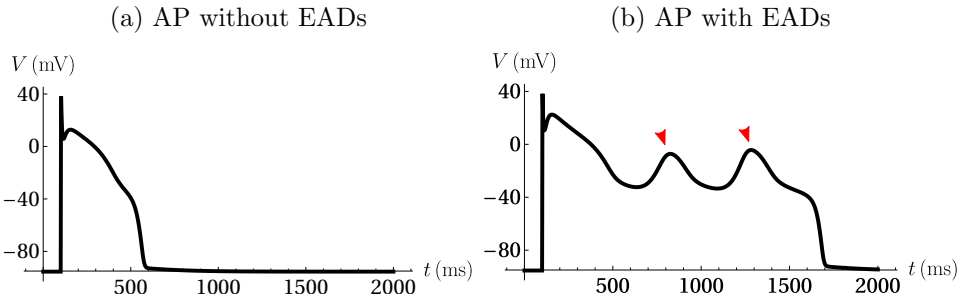


**Figure 1.** *EADs in simulated cardiac APs. Cardiac APs can exhibit EADs in response to changes in chemical environment and ion channel expression.* (a) *A simulated cardiac AP without EADs.* (b) *An AP exhibiting two EADs (red arrow markers) has a significantly prolonged duration.*

ing [22, 23, 43, 45]. Two studies in particular analyzed a three-variable model by decomposing it into a two-dimensional slow subsystem and a one-dimensional fast subsystem [23, 45]. These analyses have been very informative regarding the genesis of the EADs [23], and the effects of stimulus or pacing frequency on the production of the EADs [45]. This three-variable model was, however, intentionally minimal to facilitate analysis, and is limited in its ability to match properties of actual cardiomyocytes. In particular, the minimal model produces APs spontaneously, unlike isolated myocytes, and the EADs have very small amplitude (e.g., 1–2 mV), unlike many actual EADs that can be as large as 20 mV in amplitude [28, 51]. These limitations of a minimal model motivate the use of higher-dimensional models that exhibit more of the biophysical properties of the cardiomyocytes. However, as the dimensionality is increased and the topological structure of phase space is altered, the mathematical tools used for the lower-dimensional model become increasingly difficult to apply and need to be amended.

In this article we employ slow-fast analysis to understand EAD generation in a four-dimensional variant of the Luo–Rudy 1 model [27] introduced in [43], treating two of the variables as slow and two variables as fast. We find that the EADs generated by this model are much larger than in the three-dimensional minimal model used in [45], and we also find that the singular limit analysis is inadequate for describing the dynamics underlying the EADs. Similarly to previous works, we find a folded node in the singular limit [5]. The canard solutions associated with that folded node provide for the genesis of EADs in our system. However, the location in phase space of the maximal canards is very different from that of the singular canards, and the corresponding twisting of the stable sheet of the slow manifold occurs far from the folded node singularity that gives rise to this twisting. The trajectory moves along this manifold, where the twists result in EADs.

In the intact heart, cardiomyocyte electrical activity is driven by input originating at the sinoatrial node, and in vitro studies with isolated cells have demonstrated that periodic stimulations with low frequency are more likely to induce EADs than stimuli with a higher frequency [3, 35]. The rationale for this was explained in a previous article [45], but some voltage patterns reported in the literature were not captured by the minimal model that was employed, such as alternans with pairings of APs with and without EADs (see Figure 2 of [29], Figure 2 of [3], Figure 3 of [35], and Figures 3 and 4 of [1]) and premature EAD

termination caused by a depolarizing stimulus (see Figure 7 of [10], Figure 2 of [29], and Figure 4 of [1]). These patterns are captured with the higher-dimensional model used here, and we use slow-fast and canard analysis to understand the dynamics that underlie them.

The analysis performed herein demonstrates that slow-fast analysis can be highly useful in explaining complex multiscale phenomena even far from the singular limit.

**2. The Luo–Rudy I model.** The Luo–Rudy I model [27] was one of the earliest proposed mathematical models for the electrical dynamics of ventricular cardiomyocytes. The model includes 6 voltage-dependent transmembrane ionic currents, as well as a simplified single-compartment description of intracellular $Ca^{2+}$ handling. The inward currents include a spike-producing $Na^+$ current ($I_{Na}$), a combined slow high-threshold L-type/T-type $Ca^{2+}$ current ($I_{Ca}$), and a constant conductance background current ($I_b$). The outward currents include a delayed rectifier $K^+$ current ($I_K$), an extracellular $[K^+]$-dependent $K^+$ current ($I_{K1}$), and a high-threshold $K^+$ current ($I_{Kp}$). Taken together, the Luo–Rudy I model consists of 8 coupled nonlinear ordinary differential equations.

The analysis in this paper is strictly concerned with examining the mechanisms underlying the EADs that the Luo–Rudy I model produces. While there is some debate in the literature as to whether EADs in cardiac cells are predominantly voltage driven (dependent on voltage-gated transmembrane currents) [15, 33, 39] or $Ca^{2+}$ driven (relying on the synchronization of intracellular $Ca^{2+}$-induced $Ca^{2+}$ release) [19, 20, 50], we restrict our attention to voltage-driven EADs. To this end, we reduce the order of the Luo–Rudy I model by removing the intracellular $Ca^{2+}$ component. Moreover, since the $Na^+$ current rapidly inactivates for $V > -40$ mV, i.e., $I_{Na} \approx 0$ whenever EADs occur, we also remove this current from the model.

Hence, we use the following reduced model of membrane electrical dynamics:

$$\begin{aligned} C_m \frac{dV}{dt} &= -(I_{Ca} + I_K + I_{K1} + I_{Kp} + I_b) + I_{stim}, \\ \frac{dd}{dt} &= \frac{d_\infty(V) - d}{\tau_d(V)}, \\ \frac{df}{dt} &= \frac{f_\infty(V) - f}{\tau_f(V)}, \\ \frac{dx}{dt} &= \frac{x_\infty(V) - x}{\tau_x(V)} \end{aligned} \tag{2.1}$$

with ionic currents given by

$$\begin{aligned} I_{Ca} &= g_{Ca}\, d\, f\, (V - V_{Ca}), \\ I_K &= g_K\, x\, X_{i,\infty}(V)\, (V - V_K), \\ I_{K1} &= g_{K1}\, K_{1,\infty}(V)\, (V - V_{K1}), \\ I_{Kp} &= g_{Kp}\, K_{p,\infty}(V)\, (V - V_{Kp}), \\ I_b &= g_b\, (V - V_b). \end{aligned} \tag{2.2}$$

Here, $C_m$ is membrane capacitance and $I_{stim}$ is an applied (stimulus) current. Each transmembrane ionic current is formulated using the standard Hodgkin–Huxley formalism for excitable

membranes [13, 18]. For example, in the $Ca^{2+}$ current ($I_{Ca}$), the maximal conductance, $g_{Ca}$, is a parameter; the dynamic variables $d$ and $f$ represent the fraction of open activation and inactivation gates of all voltage-gated $Ca^{2+}$ channels, respectively, and $(V - V_{Ca})$ is the driving force for ion flux, where $V_{Ca}$ is the Nernst potential for $Ca^{2+}$. The $x$ variable denotes the (slow) activation of the delayed rectifier potassium current, $I_K$. Each of the steady-state activation and inactivation functions, $j_\infty(V)$ for $j = d, f, x, X_i, K_1$, and $K_p$, is an increasing and decreasing sigmoid, respectively. Here, we have amended the notation from the original Luo–Rudy I model [27] using uppercase letters for quantities at quasi-equilibrium. The time constants, $\tau_d(V)$ and $\tau_x(V)$, are bell shaped, and $\tau_f(V)$ is strictly increasing. Their magnitudes govern how quickly the associated gating variable adapts to changes in $V$. Small and large values of $\tau_j(V), j = d, f, x$ correspond to rapid and slow variation, respectively. We refer the reader to Appendix A for the explicit expressions used to formulate each of the steady-state gating expressions and time constants.

All parameter values are identical to those used in [27], except where explicitly stated otherwise (see Appendix A). The computer programs can be downloaded from the following website: www.math.fsu.edu/~bertram/software/cardiac.

**2.1. The Luo–Rudy I model can produce EADs.** Examples of APs and APs with EADs produced by the Luo–Rudy I model are shown in Figure 2. As is common in much of the experimental and computational literature, we reduce the magnitudes of outward $K^+$ currents and increase that of the inward $Ca^{2+}$ current in order to invoke EADs. In the Luo–Rudy I model, each of the maximal conductances and reversal potentials of the $K^+$ currents are increasing functions of the extracellular $K^+$ concentration, $[K^+]_o$. Hence, reducing $[K^+]_o$ reduces the magnitudes of hyperpolarizing currents and increases the relative strengths of their outward driving forces. This simulates hypokalemia, a condition marked by unusually low $[K^+]_o$, which compromises cardiac cell function. For the simulations produced in Figure 2, we have reduced $[K^+]_o$ to 3.0 $\mu$M (from the default value 5.4 $\mu$M) and have incrementally increased the maximal conductance of the $Ca^{2+}$ current, $g_{Ca}$, from 0.09 mS/cm$^2$ to 0.123 mS/cm$^2$ in order to demonstrate the emergence of EADs.

In all cases, there is a globally attracting hyperpolarized (stable node) equilibrium of the unforced Luo–Rudy I model, which we denote $E_1$, corresponding to the rest state of the cell and a single depolarizing pulse of 70 $\mu$A/cm$^2$ is applied for 2 ms to initiate an AP. Figure 2(a) shows a cardiac AP without EADs. Figure 2(b) shows how increases in $g_{Ca}$ cause an observable delay in repolarization, which increases the AP duration (APD) (compare Figures 2(a) and 2(b)). Further increases in $g_{Ca}$ cause the cell to begin to produce large-amplitude EADs (Figures 2(c) and 2(d)), where the presence of two EADs causes a nearly 3-fold increase in the APD. These pathological voltage deflections are the focus of this study.

There are physiologically relevant parameter sets (specifically, those sets from which EADs can be generated) for which two additional equilibria of the unforced problem arise (we refer forward to Figure 4 for an illustration). One of these equilibria, denoted $E_2$, can either be a saddle or a node focus, depending on system parameters (see section 3.3). The other equilibrium, denoted $E_3$, is a saddle for all parameter values of interest.

**2.2. EADs are generic.** Cellular manipulations similar to those presented in the simulations of Figure 2 have been shown to be a robust method for eliciting EADs in isolated cardiac

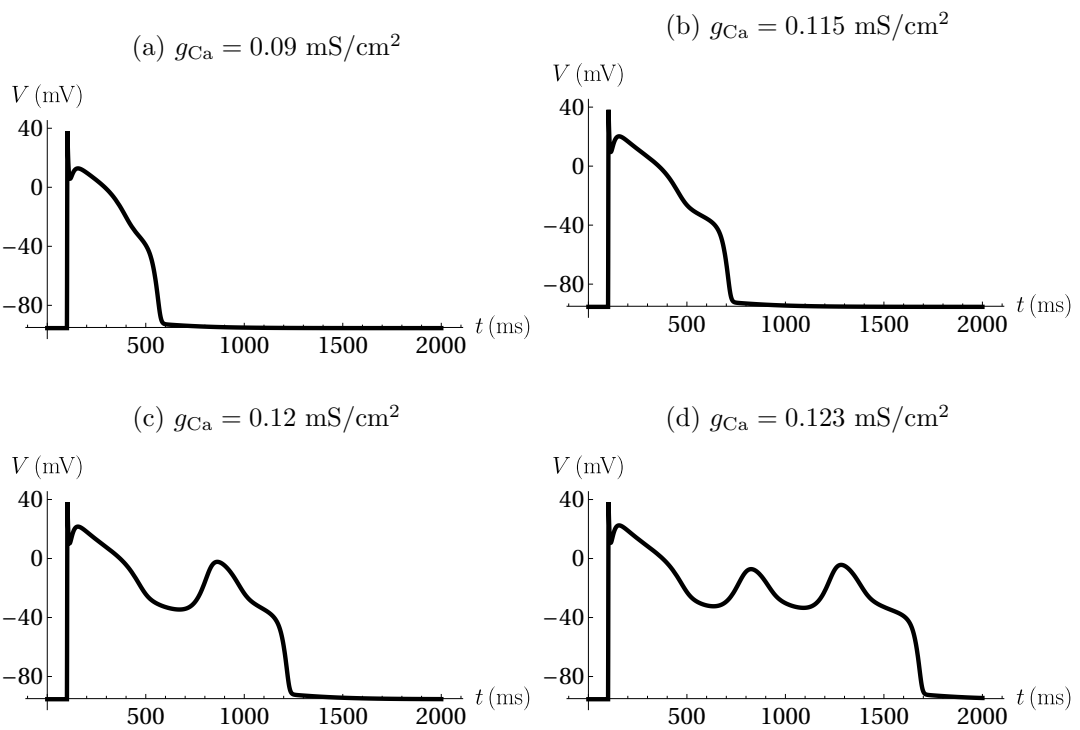


**Figure 2.** *Representative simulations from the Luo–Rudy* I *model subject to a single depolarizing pulse (at* $t = 100$ *ms) under hypokalemia (*$[K^+]_o = 3.0$ *mM). (a) A standard AP without EADs is generated. (b)–(d) Increases in the maximal* $Ca^{2+}$ *conductance,* $g_{Ca}$*, prolong the APD (b) and lead to the occurrence of EADs (c) and (d).*

cells [31, 49]. To show that the emergence of EADs demonstrated in Figure 2 is a generic phenomenon of the Luo–Rudy I model (2.1), we now examine the $(g_{Ca}, [K^+]_o)$ space over which EADs occur, shown in Figure 3. To construct this diagram, the numerical solutions of the model are determined on a $300 \times 300$ grid of parameter values. At each grid point, the behavior of the model in response to a single stimulus is categorized and color coded.

The large light green region of the $(g_{Ca}, [K^+]_o)$-plane ("No EADs") corresponds to parameter combinations of (2.1) in which APs do not exhibit EADs before returning to rest, although solutions here may have extended plateau phases (see Figure 2(b)). The large white region of the plane ("Repolarization Failure") reflects solutions that fail to repolarize after initial stimulation and instead remain at an elevated voltage. Between the "No EAD" region and the "Repolarization Failure" region is the region where EADs are produced (orange). As $[K^+]_o$ is decreased, i.e., under more severe hypokalemic conditions, the size of the $g_{Ca}$ interval where EADs are produced grows and shifts leftward. This reduces the threshold for EAD production and increases the range of $g_{Ca}$ values over which EADs occur.

The EAD region possesses additional structure. Increments in the number of EADs produced are indicated by increasingly darker shades of orange. At the darkest shade of orange 6 or more EADs are produced (we have detected more than 20 EADs for some parameter values in this region). In the diagram, we see that the region in which $n$ EADs are produced is larger than that for $n+1$ EADs. Thus, from Figure 3, we have the prediction that APs with a large

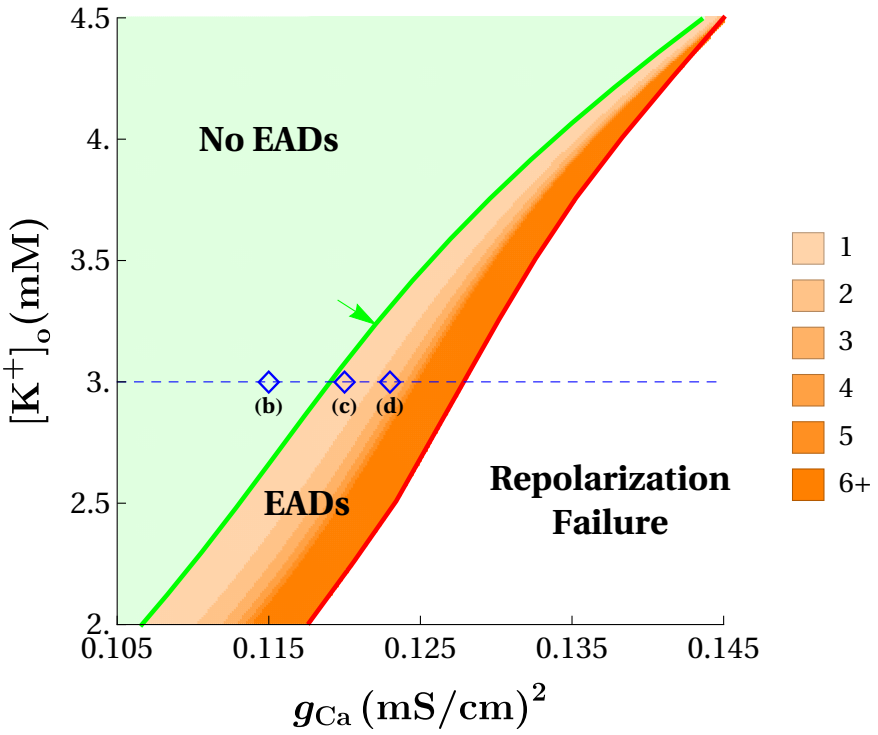


**Figure 3.** *Two parameter ($g_{Ca}$, $[K^+]_o$) diagram of EAD occurrence. Simulated responses to a single pulse reveal three distinct regions of solution behavior: No EADs (light green), EADs (orange), and Repolarization Failure (white). Within the EAD region, the number of EADs elicited is distinguished by different shades of orange (see legend). The bright green curve marking the boundary between the No EADs and EADs regions was computed using the numerical continuation and bifurcation software AUTO* [7]. *The dashed blue curve and the open blue diamonds (◇) represent the path taken in parameter space and the particular parameter values, respectively, that were used to produce panels* (b)–(d) *of Figure* 2.

number of EADs should be observed less frequently than those with a small number (or no) EADs, even in cases of hypokalemia.

The green curve (indicated by green arrow) that demarcates the transition from the No EADs region to the EADs region was computed by numerical continuation of a suitably chosen solution segment using AUTO [7]. In the case of an endogenous oscillator, as was studied in [23] and [45], this transition curve can be computed as the two-parameter locus of the first period-doubling bifurcation of the no-EAD limit cycle. With a biophysical model that requires a stimulus to evoke APs, locating this boundary is less straightforward.

Transient responses to stimuli were computed in AUTO by solving a 2-point boundary value problem with the initial endpoint fixed at the equilibrium $E_1$ and the other endpoint subject to remain at a fixed value of $V$ ($V = $ -70 mV) between the plateau and resting voltage (corresponding to the repolarization phase of the AP). Starting from a particular solution in the No EADs region, sufficient increases in the parameter $g_{Ca}$ induce a heteroclinic bifurcation connecting the stable equilibrium $E_1$ to the saddle equilibrium $E_3$. This heteroclinic bifurcation marks the boundary (in parameter space) between APs with no EADs and APs with

at least one EAD. A two-parameter continuation of this heteroclinic bifurcation produces the green boundary in Figure 3 (for details, see Appendix B). This curve is in excellent agreement with that of the simulation results, while providing a reprieve from the computational cost of numerous exploratory simulations.

The Luo–Rudy I model reproduces relevant experimental properties of EAD induction, but the information obtained through numerical simulation alone does not yield a dynamical mechanism for why or how EADs are induced. To uncover the mechanism, we now review and implement a collection of powerful analytical and numerical techniques for analyzing excitable cell models with multiscale structure. These recently developed techniques can often give a comprehensive geometric explanation for exotic oscillatory behaviors.

## 3. Geometric singular perturbation analysis.

The dynamics of the transmembrane currents that regulate cardiac cell electrical activity often evolve over disparate timescales. Geometric singular perturbation, or slow-fast analysis, takes advantage of this separation in time scales to formally decompose a system of differential equations that describes these dynamics into constituent slow and fast subsystems. The insight gleaned from analyzing each subsystem can then be pieced together to explain the behavior of the full system.

Slow-fast analysis has been used previously to analyze the dynamics of simplified versions of the Luo–Rudy 1 model, in which the timescales of some variables were modified to facilitate analysis and generate EADs [22, 43]. We demonstrate that this analysis can also be used effectively on a higher-dimensional, more biophysically accurate, version of the Luo–Rudy 1 model, without making changes to the timescales of the variables.

### 3.1. The multitimescale structure of the Luo–Rudy I model.

Dimensional analysis of (2.1) was performed by averaging over the EAD-containing AP of Figure 2(d) to obtain mean timescales of the variables (see Appendix C). This leads to the following dimensionless version of the Luo–Rudy I model:

$$
\begin{aligned}
\epsilon \frac{\mathrm{d}v}{\mathrm{d}t_s} &= -(\overline{I}_{\mathrm{Ca}} + \overline{I}_{\mathrm{K}} + \overline{I}_{\mathrm{K1}} + \overline{I}_{\mathrm{Kp}} + \overline{I}_{\mathrm{b}}),\\
\frac{\epsilon}{r}\frac{\mathrm{d}d}{\mathrm{d}t_s} &= \frac{d_\infty(v) - d}{\tilde{\tau}_d(v)},\\
\frac{\mathrm{d}f}{\mathrm{d}t_s} &= \frac{f_\infty(v) - f}{\tilde{\tau}_f(v)},\\
\frac{\mathrm{d}x}{\mathrm{d}t_s} &= \frac{\bar{\tau}_f}{\bar{\tau}_x}\frac{x_\infty(v) - x}{\tilde{\tau}_x(v)},
\end{aligned}
\tag{3.1}
$$

where $\epsilon := \frac{C_m/G_{\mathrm{tot}}}{\bar{\tau}_f} \approx 0.007 (\ll 1)$ is the small perturbation parameter, $r := \frac{C_m/G_{\mathrm{tot}}}{\bar{\tau}_d} \approx 0.05$, $G_{\mathrm{tot}}$ is the sum of maximal conductances, $g_x$, for $x \in \{\mathrm{Ca}, \mathrm{K}, \mathrm{K1}, \mathrm{Kp}, \mathrm{b}\}$, from (2.2), and the right-hand sides of (3.1) are $\mathcal{O}(1)$ with respect to $\epsilon$. The voltage, $V$, is superfast with mean timescale $\tau_V \approx 1$ ms. The activation variable, $d$, for $I_{\mathrm{Ca}}$ is fast with mean timescale $\bar{\tau}_d \approx 30$ ms. The inactivation variable, $f$, for $I_{\mathrm{Ca}}$ is slow with mean timescale $\bar{\tau}_f \approx 173$ ms. The activation variable, $x$, for $I_{\mathrm{K}}$ is superslow with mean timescale $\bar{\tau}_x \approx 561$ ms.

The dimensionless system (3.1) is used here as a tool for formal comparison of the different timescales present in the model. Both $\epsilon$ and $r$ are proportional to $C_m$, so a change in the value

of $C_m$ results in a proportionate change in $\epsilon$ and $r$. All further analysis, including figures, will be presented in terms of the original model variables and parameters.

With four timescales one has some discretion on how the variables are grouped as either fast or slow. Previous analyses of Luo–Rudy I-derived models have taken one of two approaches: (1) reduce the model complexity by assuming that $d$ adjusts instantaneously to variations in $V$ before examining EADs as canard-induced mixed-mode oscillations (MMOs) of a system with 1 fast and 2 slow variables [23, 45], or (2) treat $x$ as the sole slow variable and use the traditional slow-fast decomposition to explain EADs as initiated and terminated by Hopf and homoclinic bifurcations, respectively, of the planar fast subsystem [22]. To facilitate the slow-fast decomposition in the latter approach, the authors of [43] decreased the timescale of the $d$ variable 10-fold and increased the timescale of the $x$ variable 10-fold. In the present work, we choose a novel splitting of variables that treats $(V, d)$ as the fast subsystem and $(f, x)$ as the slow subsystem, without changing the values of the timescales. We show that this (2,2)–fast-slow splitting is sufficient for understanding the phenomena of interest; a 3-timescale splitting is not necessary.

With this splitting, the *fast subsystem* is

$$\begin{aligned} C_m \frac{\mathrm{d}V}{\mathrm{d}t} &= -(I_{\mathrm{Ca}} + I_{\mathrm{K}} + I_{\mathrm{K1}} + I_{\mathrm{Kp}} + I_{\mathrm{b}}), \\ \frac{\mathrm{d}d}{\mathrm{d}t} &= \frac{d_\infty(V) - d}{\tau_d(V)}, \\ \frac{\mathrm{d}f}{\mathrm{d}t} &= 0, \\ \frac{\mathrm{d}x}{\mathrm{d}t} &= 0, \end{aligned} \tag{3.2}$$

which is a two-dimensional (2D) approximation of (2.1) in which the slow variables are assumed to be constant. The *slow subsystem* is

$$\begin{aligned} 0 &= -(I_{\mathrm{Ca}} + I_{\mathrm{K}} + I_{\mathrm{K1}} + I_{\mathrm{Kp}} + I_{\mathrm{b}}), \\ 0 &= \frac{d_\infty(V) - d}{\tau_d(V)}, \\ \frac{\mathrm{d}f}{\mathrm{d}t} &= \frac{f_\infty(V) - f}{\tau_f(V)}, \\ \frac{\mathrm{d}x}{\mathrm{d}t} &= \frac{x_\infty(V) - x}{\tau_x(V)}, \end{aligned} \tag{3.3}$$

which is a 2D approximation of (2.1) in which the fast variables are assumed to be at their steady states.

The fast and slow subsystems, (3.2) and (3.3), are two different singular ($\epsilon \to 0$) approximations of (2.1), which provide nonoverlapping information about the dynamics of the model. The aim of our slow-fast analysis then is to analyze these simpler 2D subsystems and concatenate their information to explain the genesis and properties of EADs.

**3.2. The fast subsystem lacks an EAD-generating mechanism.** The 2D surface of equilibria of the fast subsystem is called the *critical manifold*. The $V$ and $d$ equations for the fast

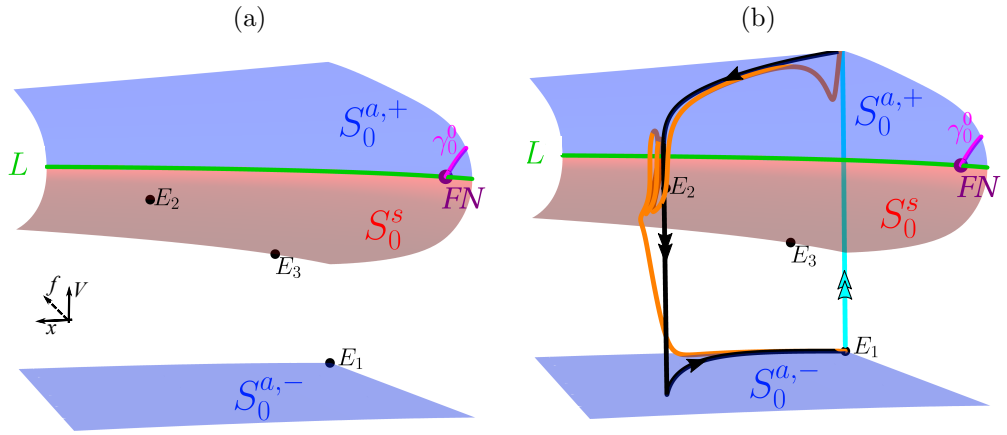


**Figure 4.** *Critical manifold and trajectories with a* (2,2)*–slow-fast splitting of variables.* (a) *The critical manifold is folded along* $L$ *(green) with upper and lower attracting sheets,* $S_0^{a,\pm}$ *(blue surfaces), and a middle unstable sheet of saddle-type equilibria,* $S_0^s$ *(red surface). Note that the sheets* $S_0^s$ *and* $S_0^{a,-}$ *are also joined, outside of the relevant domain, by a fold curve (not shown). The full four-dimensional (4D) system* (2.1) *has a stable node,* $E_1$*, which serves as the cellular rest state, a stable node focus,* $E_2$*, and unstable saddle,* $E_3$*. The slow subsystem has a folded node (FN; purple). The singular strong canard,* $\gamma_0^0$ *(magenta), and the fold curve* $L$ *(green) delimit the singular funnel.* (b) *Singular (black) and full system (orange) solutions are superimposed on the critical manifold. Fast and slow segments of the singular solution are distinguished by double and single arrows, respectively. The singular orbit (black) does not enter the funnel, nor does the trajectory of the full system (orange), yet the full trajectory contains small oscillations that delay fast repulsion toward* $S_0^{a,+}$*. Parameter values are* $g_{Ca} = 0.123\ mS/cm^2$ *and* $[K^+]_o = 3\ mM$*.*

subsystem are linear in $f$ and $d$, respectively, so we can express the critical manifold globally as a graph over $V$ and $x$:

$$f = \frac{-(I_{\mathrm{K}} + I_{\mathrm{K1}} + I_{\mathrm{Kp}} + I_{\mathrm{b}})}{G_{Ca}\, d_\infty(V)(V - V_{Ca})}, \qquad d = d_\infty(V). \tag{3.4}$$

The critical manifold is a cubic-shaped surface with upper and lower attracting sheets, $S_0^{a,+}$ and $S_0^{a,-}$ (Figure 4(a), blue surfaces), and a middle sheet, $S_0^s$ (Figure 4(a), red surface), of saddle-type equilibria. The stable sheet, $S_0^{a,+}$, and unstable sheet, $S_0^s$, are separated by a one-dimensional (1D) curve (Figure 4, green), $L$, of fold bifurcations. One potential mechanism for EADs is through a Hopf bifurcation of the fast subsystem, as suggested in [43] and [22]. However, in our model, there are no fast-subsystem Hopf bifurcations, ruling out this possibility.

Hence, solutions of the fast subsystem (3.2) with initial conditions in the physiologically meaningful region of phase space will converge to one of the attracting sheets in "fast" time. Once solutions of the fast subsystem are within the vicinity of an attracting sheet of the critical manifold, the dynamics are determined by the slow subsystem, which we discuss next.

**3.3. The slow subsystem reveals a folded node singularity.** In the slow subsystem, the fast variables $V$ and $d$ are slaved to the critical manifold (described by the algebraic constraints in (3.3)) by adjusting instantaneously to the motions of the slow variables $f$ and $x$ (described

by the differential equations in (3.3)). This makes the critical manifold the interface between the fast and slow subsystems: fast segments initialized away from the critical manifold rapidly converge to attracting sheets, where the slow dynamics take over and guide solutions along these sheets.

The slow subsystem can have two types of singularities: ordinary or folded. The ordinary singularities correspond exactly to the equilibria, $E_1$, $E_2$, and $E_3$ of the unforced problem. The ordinary equilibrium, $E_1$, is a stable node for all parameter values of interest. However, the equilibria, $E_2$ and $E_3$, are both saddle points. The saddle $E_2$ has 2 positive and 2 negative eigenvalues, while the saddle $E_3$ has 3 negative and 1 positive eigenvalue over the relevant parameter sets.

It can be shown (see Appendix E) that the slow subsystem possesses a *folded node singularity* [42] on the fold curve (Figure 4, purple marker). Associated with the folded node are a pair of special solutions of the slow subsystem, called the *singular strong canard* (Figure 4(a); $\gamma_0^0$) and the *singular weak canard*, corresponding to the strong and weak eigendirections of the folded node (see Appendix E for details). The region of $S_0^{a,+}$ bounded below by the fold curve, $L$, and above by the singular strong canard, $\gamma_0^0$, is a subset of the basin of attraction of the folded node called the *singular funnel*. Solutions of the slow subsystem with a phase point inside the singular funnel pass through the folded node with finite speed, cross from $S_0^{a,+}$ to $S_0^s$, and follow $S_0^s$ for $\mathcal{O}(1)$ time on the slow timescale. Such solutions are known as *singular canards* and their persistence under small perturbations ($0 < \epsilon \ll 1$) gives rise to small oscillations that are characteristic of EADs.

Canard-induced small oscillations emerge in the vicinity of the folded node, and in prior studies it has been shown that these are responsible for EADs [22, 45]. Thus, in phase space, EADs are typically generated near a folded node of the desingularized slow subsystem.

**3.4. The singular solution predicts No EADs.** We can now use the information gained from the two subsystems to construct a singular approximation of the EAD-containing solution from Figure 2(d) and examine its behavior in light of the singular geometry and the folded node. Since the rest state of the full system is a stable equilibrium ($E_1$), APs are generated only in response to a sufficiently large stimulus. (This is in contrast to some prior studies in which the system was oscillatory [22, 23, 35, 45].)

Figure 4(b) shows the transient response of the model cell to a sufficiently strong stimulus in the full 4D system (orange) as well as the corresponding singular solution trajectory (black), with both solutions projected into $(f, x, V)$-space and superimposed on the critical manifold. Under the flow of the full system (2.1), the initial impulse (cyan segment, double arrows) ejects the solution from the stable rest state, $E_1$, toward, and even beyond, $S_0^{a,+}$. Following the stimulus, the solution returns to and slowly moves along $S_0^{a,+}$ toward the fold curve, $L$. The solution then crosses $L$ and exhibits two oscillations about $L$ before being rapidly repelled toward $S_0^{a,-}$. These oscillations are the EADs seen in Figure 2(d). After this, the trajectory returns to $S_0^{a,-}$ and slowly approaches the stable rest state, $E_1$.

Under the singular limit, we construct an analogous singular solution trajectory as a concatenation of solution segments from the separate fast and slow subsystems. As in the nonsingular case, a sufficiently strong stimulus segment (cyan, double arrow) injects the solution into the basin of attraction of $S_0^{a,+}$, outside of the singular funnel. Once on $S_0^{a,+}$, the

slow subsystem describes the slow drift (black curve, single arrow) along the critical manifold toward the fold curve, $L$. When $L$ is reached, the orbit exhibits classical relaxation oscillation-like behavior—switching to the fast dynamics (described by the fast subsystem)—and transitions rapidly (black, double downwards arrows) to the lower attracting sheet of the critical manifold, $S_0^{a,-}$. Once on $S_0^{a,-}$, the trajectory (single arrow) is again described by the slow subsystem as it returns to rest, $E_1$, completing the construction.

Surprisingly, the equilibrium $E_2$ changes stability, from a saddle point for $C_m = 0\,\mu\text{F/cm}^2$ to a stable focus with two complex eigenvalues having negative real parts for $C_m = 1\,\mu\text{F/cm}^2$, in contrast to the typical preservation of asymptotic stability away from the singular limit. More specifically, the equilibrium $E_2$ undergoes a subcritical Hopf bifurcation with respect to changes in $C_m$ (see Appendix F). The unstable limit cycles that emerge from the Hopf bifurcation do not appear to influence the local canard dynamics. Moreover, even though $E_2$ is stable for $C_m = 1\,\mu\text{F/cm}^2$, the full solution (orange) shown in Figure 4(b) never enters its basin of attraction. However, the repolarization failure shown in Figure 3 results from trajectories entering the basin of attraction of $E_2$.

When comparing the singular orbit to that of the full system, it is evident that the singular solution retains many of the important properties of the full solution, such as the plateau phase characteristic of cardiac APs, the rapid repolarization of the cell following the plateau, and the slow return to the rest state following repolarization. In the singular orbit, however, the two small EAD oscillations about $E_2$ are lost. It is most notable that neither the singular orbit nor the full system orbit approach the folded node or enter the singular funnel.

The large $\mathcal{O}(1)$ distance in the $x$-coordinate in Figure 4(b) between the folded node and the two large EAD oscillations (about $E_2$) is a significant departure from prior analyses of canard-induced EADs [23, 45]. Hence, the singular solution alone gives us no information as to how these EAD oscillations are generated under the full 4D flow. To understand this, we must examine how the critical manifold unfolds into locally invariant *slow manifolds* away from the singular limit.

## 4. EADs are produced by twisted slow manifolds.

The previous section demonstrated that the singular limit is ill-suited for explaining the dynamics underlying EADs in the 4D Luo–Rudy I model. However, the configuration of the critical manifold, its folded structure, and the presence of a folded node singularity allow for the possibility of canard-induced oscillatory dynamics in the fully perturbed problem. We now investigate how the full system geometry unfolds from the structures of the singular approximation to generate EADs.

### 4.1. The twisted region of the slow manifolds unfolds toward larger values of $x$.

Fenichel theory [8, 16] guarantees that, under sufficiently small perturbations ($0 < \epsilon \ll 1$), subsets of the critical manifold that are outside the vicinity of the fold curve, $L$, perturb smoothly to nearby locally invariant slow manifolds of the perturbed flow. In fact, the normal attraction/repulsion properties of these sets is key in guaranteeing that they persist under perturbation. As we have seen, however, the EADs occur in the vicinity of $L$—precisely where Fenichel theory breaks down. Canard theory provides a theoretical basis for extending the Fenichel results into the neighborhood of the fold and, specifically, the folded node, in order to explain the complex oscillatory behavior that emerges as we move away from the singular limit [21].

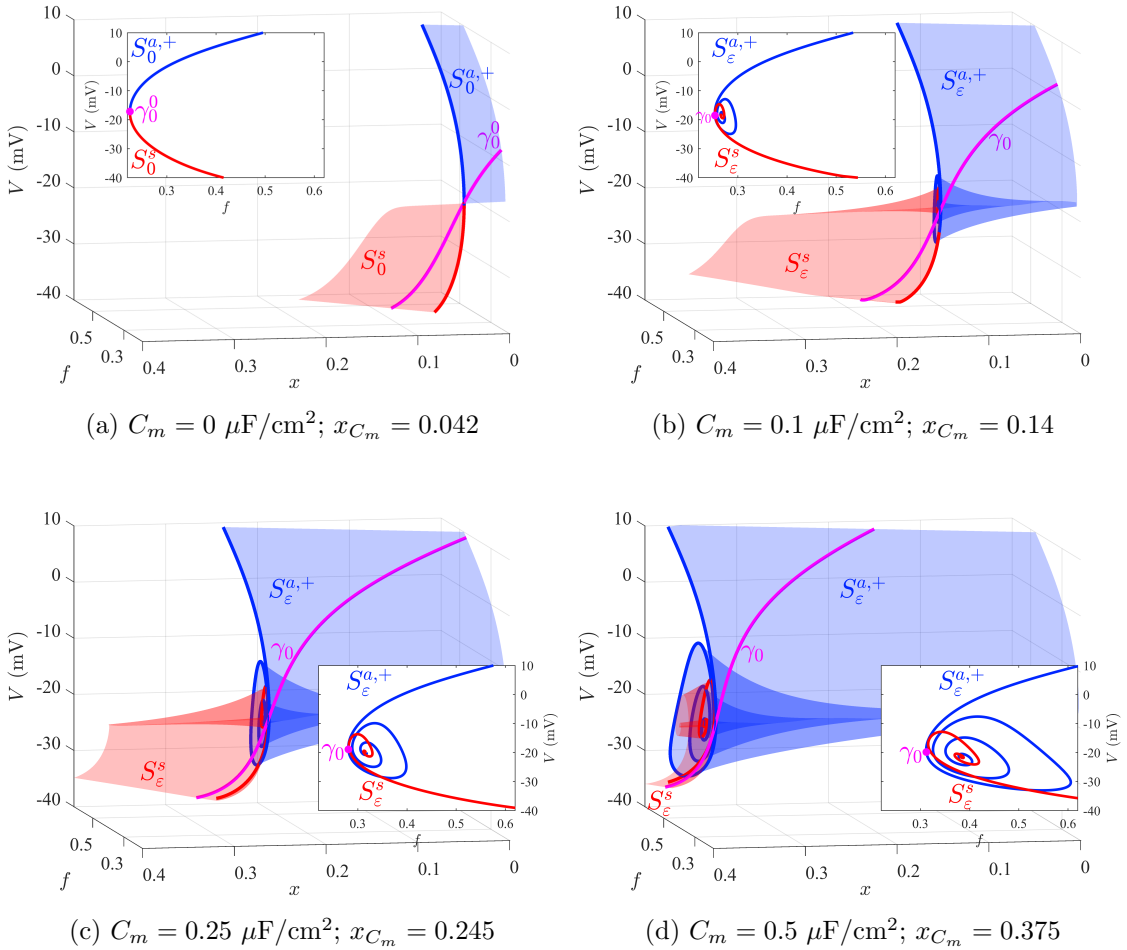


**Figure 5.** *Unfolding of the critical manifold and singular strong canard. The critical manifold* (a) *perturbs to locally twisted (and locally invariant) slow manifolds, $S_\epsilon^{a,+}$ (blue surface) and $S_\epsilon^s$ (red surface) whose funnel region, delineated by the primary strong canard $\gamma_0$ (magenta curve), unfolds toward larger values of $x$ as capacitance, $C_m$, is increased* (b)–(d). *The insets show projections of the intersections of the slow manifolds and the strong canard with the hyperplane, $\sum_{C_m}$, into $(f, V)$-space. The capacitance, $C_m$, and the value of the fixed hyperplane coordinate, $x_{C_m}$, are given under each panel.*

Canard theory holds that in the neighborhood of the folded node, away from the singular limit, $S_0^s$ and the singular funnel of $S_0^{a,+}$ perturb to locally twisted slow manifolds, $S_\epsilon^s$ and $S_\epsilon^{a,+}$, respectively (see Figure 5), with the weak canard acting as axis of rotation [6, 42, 47]. In the system analyzed in prior studies of EADs, with two slow and one fast variable, local twisting of the slow manifolds in the vicinity of the folded node induced a finite number of transverse intersections of the attracting and repelling slow manifolds [45]. The curves along which the 2D slow manifolds intersect in this case are called *maximal canards*. However, in our system, with two slow and two fast variables, the transverse intersections of $S_\epsilon^s$ and $S_\epsilon^{a,+}$ are no longer 1D curves (i.e., solution trajectories) generically. Generic intersections of 2D

slow manifolds in $\mathbb{R}^4$ are isolated points. In light of this, we follow [12] and, instead, define maximal canards as solutions of (2.1) that follow $S_\epsilon^s$ for the largest $\mathcal{O}(1)$ times on the slow timescale.

The structure of the slow manifolds, $S_\epsilon^{a,+}$ (blue) and $S_\epsilon^s$ (red), over a sequence of increasing values of the membrane capacitance, $C_m$ (recall that $\epsilon \propto C_m$), is shown in Figure 5. In each case, the corresponding strong canard ($\gamma_0$) is superimposed atop the slow manifold and the region of the phase space in view is fixed. The methods for computing slow manifolds and canards in $\mathbb{R}^4$ are detailed in [12].

For ease of visualization, the slow manifolds in each panel have only been computed up to the hyperplane $\sum_{C_m} := \{(V, d, f, x) \in \mathbb{R}^4 : x = x_{C_m}\}$, where the choice of $x = x_{C_m}$ varies with $C_m$. The slow manifolds and the strong canard are then projected into $(f, x, V)$-space. Insets show the intersections of the slow manifolds and the strong canard with the chosen hyperplane, $\sum_{C_m}$, in the $(f, V)$-plane. Although the curves of intersection of $S_\epsilon^{a,+}$ (blue) and $S_\epsilon^s$ (red) with the hyperplane appear to intersect one another, this is an artifact of projecting the 4D dynamics into lower-dimensional spaces. For each value of $C_m$ we have discretion over the value of the hyperplane coordinate, $x_{C_m}$, up to which we compute the slow manifolds. We choose to standardize the reference frame across different values of $C_m$ by selecting the $x_{C_m}$ value that (approximately) aligns the intersection point of the strong maximal canard with the first turning point of $S_\epsilon^{a,+}$.

Two important observations can be made from the unfolding of the slow manifolds. First, as $C_m$ is increased, the local twisting of the slow manifolds moves to larger $x$-values in phase space. Specifically, there is a 10-fold increase in the $x$-coordinate of where twists are centered for an increase from $C_m = 0\,\mu\text{F/cm}^2$ to $C_m = 0.5\,\mu\text{F/cm}^2$ (compare $x_{C_m}$ from Figures 5(a) and 5(d)). Second, the amplitudes of the twists grow significantly as $C_m$ is increased ($\sim$20 mV in amplitude). Such a large-amplitude twisted structure would be capable of producing the large EADs seen in Figures 2(c) and 2(d). Both of these observations are in contrast with the previously studied EAD models, where the unfolding of the slow manifolds occurs near the folded node and produces local twisting of relatively small amplitude.

### 4.2. There are large shifts in the strong canard and funnel away from the singular limit.

To show that the unfolding of the singular limit—and the canards this unfolding produces—are responsible for the generation of EADs, we begin by examining the unfolding of the strong canard up to $C_m = 1\ \mu\text{F/cm}^2$. This is important since it forms the upper boundary for the funnel that determines whether canard solutions, with twisting trajectories, are produced.

Figure 6 depicts how the strong canard, superimposed on the critical manifold, moves significantly for increasing values of $C_m$. We remind the reader that the sheets of the critical manifold perturb to slow manifolds, which change their location in phase space with increases in $C_m$. However, the positions of the equilibria, $E_1$–$E_3$, remain fixed under variation in $C_m$. For $C_m = 0\,\mu\text{F/cm}^2$, the singular strong canard passes from $S_0^{a,+}$, through the folded node ($FN$, purple marker), and onto $S_0^s$. Away from the singular limit, for $C_m = 0.5\,\mu\text{F/cm}^2$ and $C_m = 1\,\mu\text{F/cm}^2$, the strong canard shifts leftward toward larger values of $x$, in the direction of $E_2$. Since this is a boundary of the funnel, the funnel exhibits a similar leftward shift. The orbit of the system with $C_m = 1\,\mu\text{F/cm}^2$ enters along the attracting upper sheet to the right of the strong canard, and thus, for this capacitance value, enters the funnel. This suggests

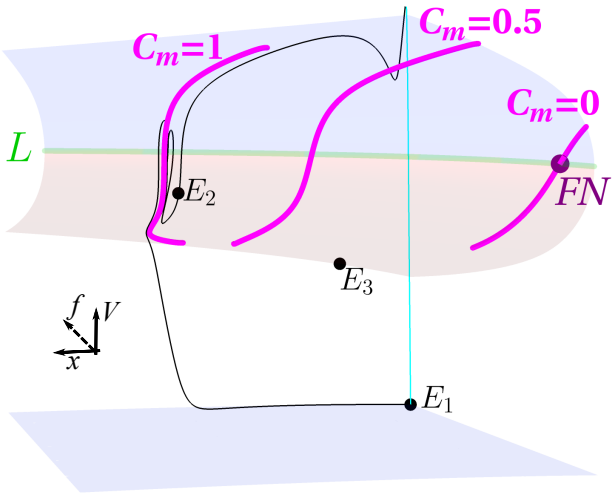


**Figure 6.** *A trajectory exhibiting EADs enters the funnel region delimited by the strong canard. The strong canard (magenta curve) moves leftward toward $E_2$ as $C_m$ is increased from 0 to 1 $\mu F/cm^2$, implying concurrent leftward movement of the twisted slow submanifold of $S_\epsilon^{a,+}$. The critical manifold and the folded node (FN, purple) are included for reference. With $C_m = 1$ $\mu F/cm^2$, the default capacitance value, the EAD-containing trajectory (thin black curve) falls within the funnel (to the right of the strong canard).*

that the EADs present in the trajectory may be due to canards formed by the twisted slow submanifold of $S_\epsilon^{a,+}$.

**4.3. EADs are induced by canards.** To have further confidence that the two EADs exhibited by the system are due to canards, we look at predictions made by canard theory regarding the number of expected small oscillations. According to this theory, the funnel can be partitioned into rotational sectors that dictate the number of small oscillations produced in an orbit by entering a particular sector, reflecting the effects of the local twisting of the slow manifolds [12, 42]. In particular, solutions entering the rotational sector between the strong canard, $\gamma_0$, and the next maximal canard, $\gamma_1$—termed the first *secondary maximal canard*—exhibit one small oscillation before being repelled toward the lower attracting sheet, $S_\epsilon^{a,-}$. Solutions entering the rotational sector between the first and second secondary maximal canards, $\gamma_1$ and $\gamma_2$, respectively, exhibit two small oscillations. For each subsequent rotational sector, an additional small oscillation is added to entrant solution trajectories before they are repelled toward $S_\epsilon^{a,-}$.

If the EADs are produced through the canard mechanism, then we predict that the trajectory with two EADs should enter the funnel between $\gamma_1$ and $\gamma_2$. To test this prediction, Figure 7 focuses in on two regions of the $(f, x, V)$-phase space: (a) the region near where the solution settles to a particular rotational sector along $S_\epsilon^{a,+}$ following the stimulus, and (b) the region where the EADs occur. Both regions show the first three maximal canards along with the superimposed trajectory ($\Gamma$, in black). As predicted, Figure 7(a) shows that the solution is injected onto the upper attracting sheet along the rotational sector (shaded blue) between

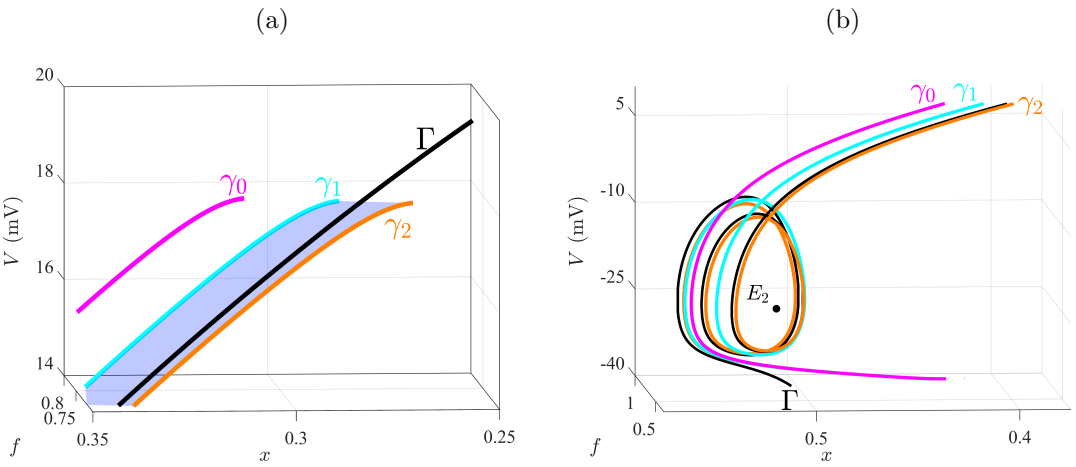


**Figure 7.** *EADs are canard-induced oscillations. Two distinct regions of the $(f, x, V)$-phase space show that EAD number is determined by the rotational sector into which a solution enters.* (a) *Magnified view of the region where the solution ($\Gamma$, black curve) begins to follow the upper slow manifold. In this region, the solution trajectory is shown to lie within the rotational sector (blue shaded section) between the maximal canards $\gamma_1$ (cyan curve) and $\gamma_2$ (orange curve).* (b) *As predicted by canard theory, the trajectory undergoes two EADs before being repelled toward $S_\epsilon^{a,-}$.*

$\gamma_1$ (cyan curve) and $\gamma_2$ (orange curve). Panel (b) shows how the maximal canards extend into, and beyond, the region where EADs occur and that the solution, $\Gamma$, indeed follows the maximal canards very closely, exhibiting two oscillations before being repelled toward $S_\epsilon^{a,-}$. With this, it becomes evident that the EADs produced by the Luo–Rudy I model are induced by canards.

Thus far, our analysis has focused on the response of the Luo–Rudy I model to a single depolarizing pulse. We found that the transient EADs produced in response to this stimulus are due to the presence of canards. We next turn to the more physiological situation in which the cell is pulsed periodically.

**5. Canards explain the effects of pacing cycle length on the existence and regularity of EADs.** Ventricular cardiac cells, under healthy conditions, require repetitive depolarizing stimuli in order to fulfill their proper function. Experimental studies of cardiac cells have found that ventricular electrical rhythms—measured using diagnostics such as the APD and diastolic interval (DI)—are highly dependent on the length of time between these depolarizing pulses, termed the *pacing cycle length* (PCL). The APD, DI, and PCL are (generally) related by the formula: APD + DI = PCL. In particular, it has been shown experimentally that EADs are more likely to occur and are often more numerous under long PCLs than under short PCLs [3, 35]. In addition, intermediate ranges in PCL are often shown to elicit more irregular EAD behavior, such as alternation of APs exhibiting different numbers of EADs. This alternation manifests as periodic/aperiodic fluctuations in APD from beat-to-beat. These beat-to-beat fluctuations in APD are called APD *alternans* [9, 27, 32, 39]. In this section, we reproduce these behaviors in the model and explain them using slow-fast analysis.

**5.1. Luo–Rudy I reproduces the dependence of EADs on the PCL.** Previous mathematical analysis of a minimal model from [35] revealed that canards underlie the relationship between EAD production and the PCL [45]. That is, canards were shown to both determine the number of EADs elicited under a given PCL and to be the source of the irregular alternan behavior seen at intermediate PCLs. However, the model that was used in this analysis was an endogenous oscillator, whereas standard ventricular cardiac cells—even those that exhibit repeated EADs under periodic stimuli—remain at rest in the absence of stimuli. We therefore examine how the more biophysically realistic Luo–Rudy I model responds to a range of PCLs, and examine the role that canards play in determining these responses.

We begin by examining the asymptotic responses of the model to periodic pacing using a range of PCLs. Figure 8 shows a bifurcation diagram of APD versus PCL (Figure 8(a)) along with representative voltage traces for each response type (Figures 8(b)–8(g)). The APD is calculated as the total time that a solution segment spends above 90% of the resting voltage level, $V_{\text{rest}}$. Farey sequence notation, $L^s$, is used to denote the type of MMO behavior obtained on each branch of solutions, where $1^2$, for instance, indicates that one large amplitude ($L = 1$) oscillation is followed by two small amplitude ($s = 2$) oscillations (EADs) before the model cell repolarizes. Period-$n$ behavior is denoted by $L_1^{s_1} L_2^{s_2}, \ldots, L_n^{s_n}$ with $n$ coexisting branches of the same color for a given range of PCL. For example, the $1^2 1^0$ family in Figure 8(a) indicates a period-2 orbit with two APs: one with two EADs and one with no EADs. This is represented in the diagram as two curve segments of the same color (brown, in this case). The lower curve gives the APD of the AP with no EADs, while the upper curve gives the APD of the AP with two EADs.

The bifurcation diagram shows that the model reproduces essential features of the experimentally observed relationship between EADs and the PCL. APs without EADs (see Figure 8(b)) are the global attractor of the forced system under short PCLs (cf. Figure 8(a), red branch: PCL $\in [650, 924]$ ms), while APs with two EADs (see Figure 8(g)) are the global attractor under sufficiently long PCLs (cf. Figure 8(a), purple branch: PCL $\in [2139, 2200]$ ms). However, between these two extreme ranges of PCL, the model produces behaviors not produced by the minimal model [35], and these behaviors are the focus of the analysis below.

One behavior produced by the Luo–Rudy I model at intermediate PCls, but not the minimal model, is the premature termination of EADs by intra-AP pulses. This behavior, shown in Figure 8(c), occurs along the blue $1^{1+}$ branch in Figure 8(a) (PCL $\in [718, 1591]$ ms), and has been observed experimentally [1, 10, 29]. Along this branch, an initial stimulus triggers an AP that would contain either one or two EADs, but a second stimulus occurs during an EAD and leads to the subsequent repolarization of the model cell. We label this branch of solutions as "$1^{1+}$" MMOs because it contains more than one type of pulse-induced MMO-like signature. For shorter PCL values, this solution branch reflects APs with interrupting pulses that occur early enough during a single EAD to bear resemblance to a $1^1$ MMO signature. For longer PCL values, this branch of solutions reflects APs with interrupting pulses that occur during the repolarization phase following two EADs, which bear resemblance to a $1^3$ MMO signature. Transitions between these signatures are smooth and lack obvious boundaries. The latter $1^3$-like MMO signature is what leads to the very large APDs observed for the largest PCLs in this solution family.

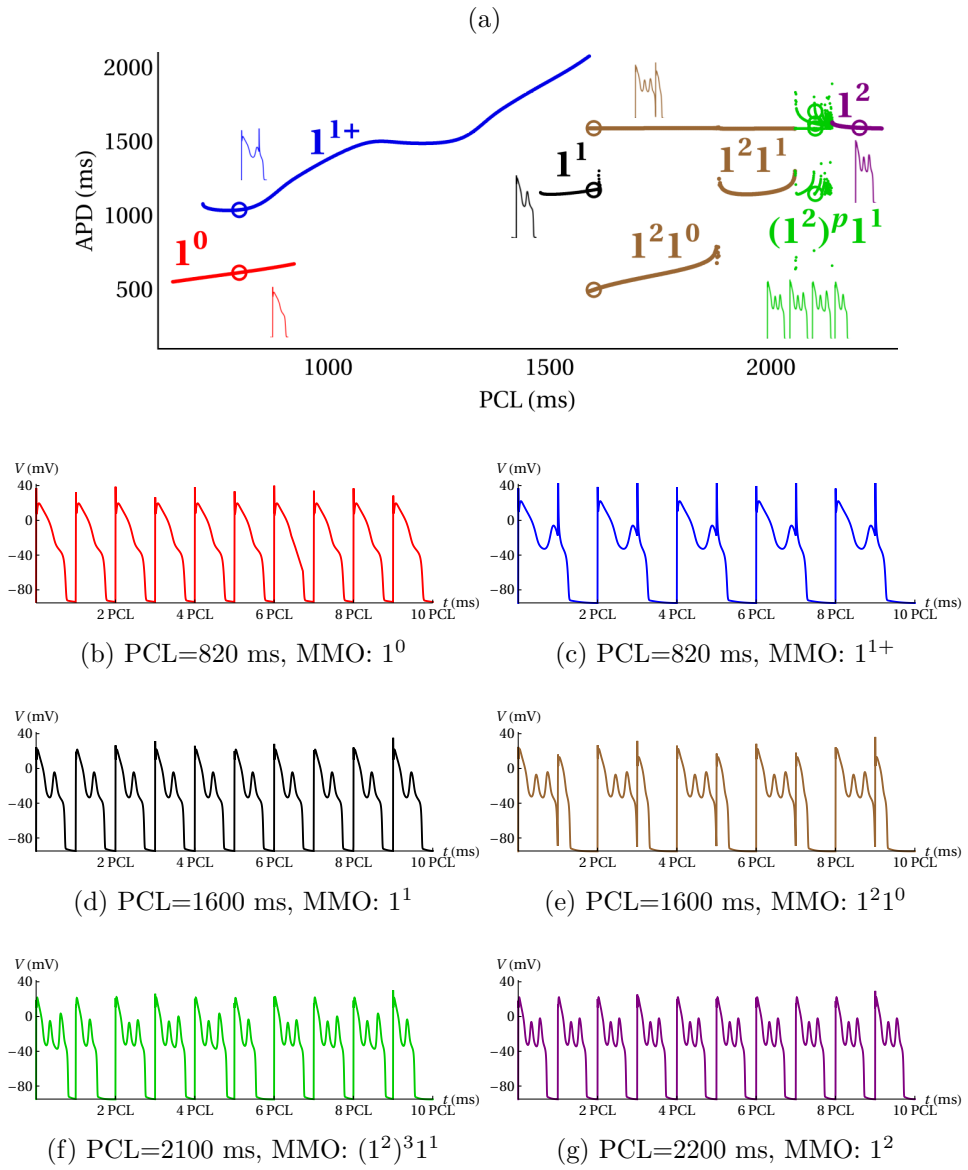


(b) PCL=820 ms, MMO: $1^0$

(c) PCL=820 ms, MMO: $1^{1+}$

(d) PCL=1600 ms, MMO: $1^1$

(e) PCL=1600 ms, MMO: $1^2 1^0$

(f) PCL=2100 ms, MMO: $(1^2)^3 1^1$

(g) PCL=2200 ms, MMO: $1^2$

**Figure 8.** *APD versus PCL bifurcation diagram with representative solutions from each behavioral regime.* (a) *Luo–Rudy* I *admits a range of PCL-dependent EAD behaviors, some of which have been reported in other cardiac models. Short PCLs (red) eliminate EADs, very long PCLs (purple) lead to periodic APs with two EADs, and intermediate PCLs can lead to rhythms with complex signatures (green). Intermediate PCLs generate myriad novel behaviors as yet unexplained in previous analyses, including pulse-induced termination of EADs (blue), EAD alternans that pair APs with and without EADs (brown), and bistability between different regimes of solution behavior (e.g., stimuli with* $PCL = 820$ *ms can either eliminate EADs or cause EADs that are terminated by an interrupting pulse).* (b)–(g) *Voltage time-courses from each behavioral regime are shown and subcaptioned by the PCL used to elicit such behavior.*

A second behavior produced by the Luo–Rudy I model, but not the minimal model, is EAD alternans that pair APs with and without EADs (Figure 8(e)). This behavior has also been reported in experiments [1, 3, 29, 35]. In the bifurcation diagram (Figure 8(a)), it occurs along the brown $1^2 1^0$ branch (PCL $= [1591, 1878]$ ms). For larger PCL values, this branch of solutions also contains alternans that pair APs with one and two EADs ($1^2 1^1$ branch; PCL $\in [1878, 2055]$ ms). Thus, for the PCLs corresponding to the brown APD branches in Figure 8(a), an initial stimulus triggers an AP with two EADs that repolarizes before a second stimulus produces either a standard AP ($1^2 1^0$; see Figure 8(e)) or an AP with a single EAD ($1^2 1^1$; not shown).

Figure 8(a) also shows that there is a range of pacing frequencies that can lead to "dynamical chaos" (Figure 8(a), green $(1^2)^p 1^1$ branch; see Figure 8(f) for a representative time series). This phenomenon was first described and examined in detail in [35]. We refer the reader to [45] for an explanation of the mechanisms underlying this behavior. However, its existence in the present context gives evidence for the genericity of this phenomenon in model cardiac cells and also shows that the Luo–Rudy I model does well at subsuming previous findings.

Finally, there are two intervals of the bifurcation diagram exhibiting bistability, indicated by the coexistence of solution families with different MMO signatures and represented by different colors. In the first bistable interval, PCL $\in$ [718, 924] ms, solutions without EADs (Figure 8(a), red $1^0$ branch; see Figure 8(b)) and those that experience pulse-induced EAD termination (Figure 8(a), blue $1^{1+}$ branch; see Figure 8(c)) are both stable attractors. In the second bistable interval, PCL $\in$ [1480, 1614] ms, solutions with one EAD (Figure 8(a), black $1^1$ branch; see Figure 8(d)) are bistable with either those that exhibit pulse-induced EAD termination (blue: "$1^{1+}$") or those that contain period-2 EAD alternans (brown: "$1^2 1^0$"; see Figure 8(e)). This bistability was not observed in the minimal model [35] and, to our knowledge, it has not been investigated experimentally.

**5.2. PCL determines where solutions are ejected along $S_\epsilon^{a,-}$.** To understand the range of behaviors produced at different PCLs, we begin by relating the solution behavior depicted in the APD versus PCL bifurcation diagram to the underlying flow in phase space. The analysis in [45] showed that the PCL dictates where along $S_\epsilon^{a,-}$ a solution is pulsed, which determines the rotational sector that the solution enters on $S_\epsilon^{a,+}$, and hence determines how many EADs are produced. One of the primary differences between the previously analyzed model from [35] and Luo–Rudy I is the presence of a stable hyperpolarized equilibrium, $E_1$, of the unforced problem. Because of this attractor, the system is at rest in the absence of stimuli, and the trajectory is on or near $S_\epsilon^{a,-}$ between pulses. In fact, the trajectory follows the almost-linear invariant submanifold corresponding to the weakest eigendirection of $E_1$ after a stimulus-induced AP. We refer to this almost-linear submanifold as the *curve of approach*.

We next partition this curve of approach into segments of uniform behavior upon stimulation; if a pacing stimulus is applied while the trajectory is at any point within one segment, the response will be the same (e.g., it will produce an AP with the same number of EADs). This is because, within any one segment, the stimulus injects the trajectory into the same rotational sector of $S_\epsilon^{a,+}$. Figure 9 shows how the curve of approach can be partitioned in this way. It also shows the three leading maximal canards ($\gamma_0$, magenta; $\gamma_1$, cyan; $\gamma_2$, orange), all of which are superimposed on the critical manifold. The segments of the curve of approach are

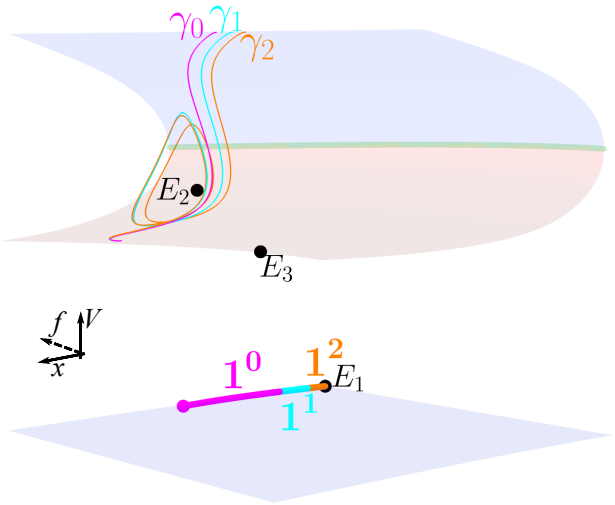


**Figure 9.** *Position on the curve of approach at the time of pulse initiation determines the number of EADs evoked. Following an AP, the solution trajectory returns to $E_1$ along a curve of approach on $S_\epsilon^{a,-}$. This is partitioned into three segments, "$1^0$" (magenta), "$1^1$" (cyan), and "$1^2$" (orange). Stimulation on segment $1^0$ injects the trajectory to the left of $\gamma_0$, outside the funnel. Stimulations on segment $1^1$ injects the trajectory into the rotational sector between $\gamma_0$ and $\gamma_1$, yielding 1 EAD. Stimulations on segment $1^2$ injects the trajectory into the rotational sector between $\gamma_1$ and $\gamma_2$, yielding 2 EADs.*

color coded using the same color scheme as that of the maximal canards in order to indicate how pulse timing determines which rotational sector a solution enters. If a trajectory in a rotational sector exhibits $n$ EADs, we say that the sector has *cardinality* $n$.

Solutions that are given a single pulse along the segment labeled $1^0$ (magenta) are injected into $S_\epsilon^{a,+}$ to the left of $\gamma_0$—outside the funnel region—and do not exhibit any EADs (the cardinality is 0). Solutions pulsed along the segment labeled $1^1$ (cyan) are injected into the rotational sector of $S_\epsilon^{a,+}$ to the left of $\gamma_1$ (and to the right of $\gamma_0$) which generates a single EAD, and solutions pulsed along the segment labeled $1^2$ (orange) are injected into the rotational sector of $S_\epsilon^{a,+}$ to the left of $\gamma_2$ (and to the right of $\gamma_1$) which generates two EADs. Hence, the boundaries between these distinguishable segments along the curve of approach in $S_\epsilon^{a,-}$ correspond to the rotational sector boundaries of $S_\epsilon^{a,+}$ delimited by the maximal canards. The reason that longer PCLs are more likely to produce EADs, or an increased number of EADs, is that the longer PCL allows the trajectory to move further along the curve of approach, entering a segment corresponding to a rotational sector with higher cardinality.

**5.3. Canards, PCL, and initial conditions underlie pulse-induced termination of EADs and EAD alternans.** We use the curve of approach presented in Figure 9 to frame our discussion of how the richer set of responses produced by the Luo–Rudy I model, as compared to the minimal model [35], are the result of complex interactions between the maximal canards, the PCL, and the point of ejection along $S_\epsilon^{a,-}$. We start by examining the responses generated by the model that have also been observed in experiments, the first of which is early termination of EADs due to intra-AP pulses.

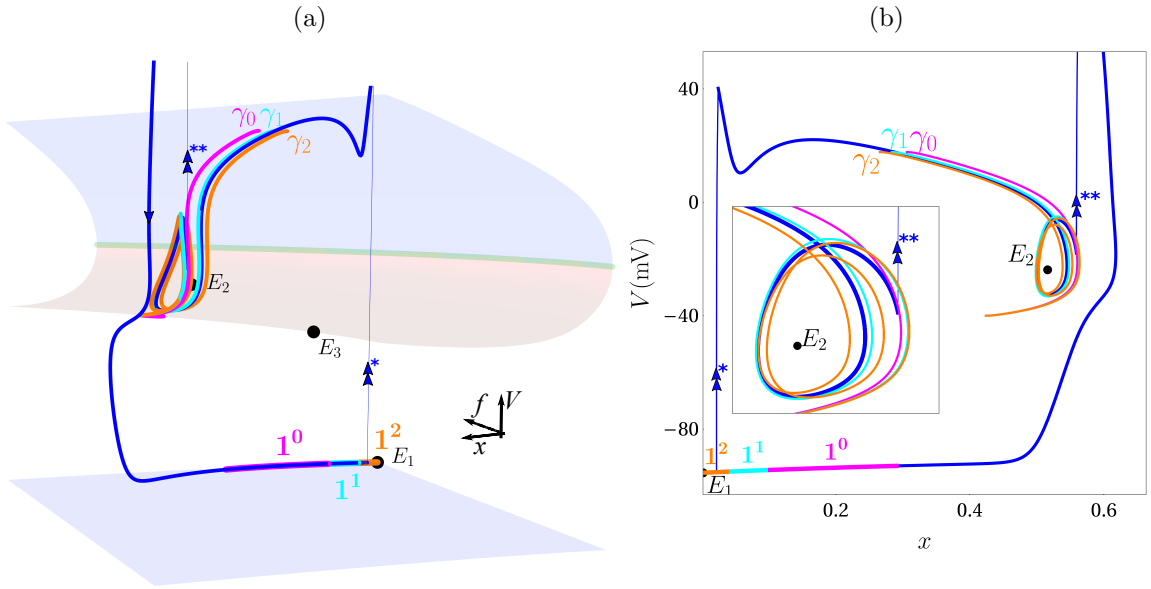


**Figure 10.** *Pulse-induced termination of EADs.* (a) *The complete solution trajectory exhibiting pulse-induced EAD termination from Figure 8(c) (blue) is superimposed, along with the three leading maximal canards ($\gamma_0$, magenta; $\gamma_1$, cyan; $\gamma_2$, orange), onto the critical manifold. The dashed line with double arrows represents a stimulus: * represents the first stimulus and ** the second.* (b) *A 2D $(x, V)$ projection with inset close-up view of the funnel.*

Figure 10 shows two different views of the solution from Figure 8(c) in $(f, x, V)$ phase space. Figure 10(a) superimposes the complete $1^{1+}$ solution (blue), along with the three leading maximal canards ($\gamma_0$, magenta; $\gamma_1$, cyan; $\gamma_2$, orange) and the partitioned curve of approach from Figure 9, onto the critical manifold. This solution is period-2 with respect to the PCL. The initial depolarizing pulse (thin blue segment, upward arrow) occurs on the bottom sheet, within the orange $1^2$ segment of the curve of approach with a cardinality of two. This solution moves along $S_\epsilon^{a,+}$ for a long time, and before it leaves the manifold a new stimulus is applied. This stimulus ejects the trajectory upward (double arrow, **) out of the funnel, where the flow then leads the solution (thick blue curve, single arrow) back to the upper sheet, outside of the funnel. The solution quickly repolarizes, but the PCL is long enough to allow the trajectory to return to the $1^2$ segment of the curve of approach before the next stimulus is applied, completing the cycle.

Figure 10(b) shows a projection of this solution and the invariant structures into the $(x, V)$-plane. The inset contains a magnified view of the region where the EADs occur to show that the EAD-terminating second stimulus occurs near the end of the first EAD within the funnel region.

We now look at the generation of EAD alternans. Specifically, we focus on the case where APs with two EADs are interleaved by APs without EADs. We find that this phenomenon is also due to the complex interactions between the maximal canards, the PCL, and the position along the curve of approach where a stimulus is applied.

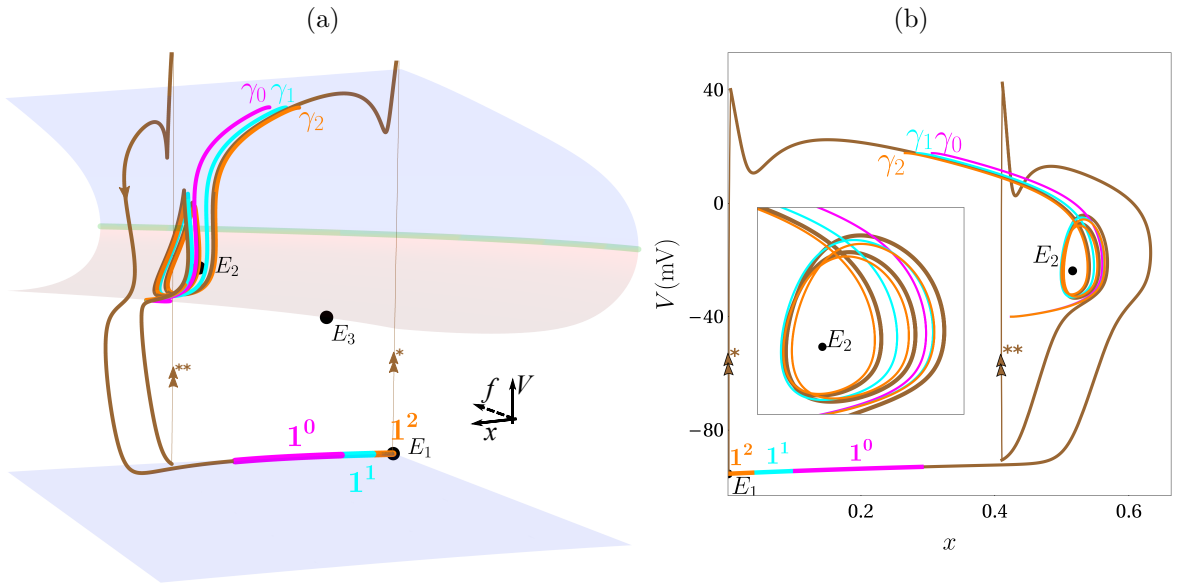


**Figure 11.** *EAD alternans can be explained in terms of canards and the PCL.* (a) *The solution trajectory projected into the* $(f, x, V)$ *phase space exhibiting* $1^2 1^1$ *EAD alternans from Figure* 8(e) *(brown) is superimposed, along with the three leading maximal canards* ($\gamma_0$, *magenta;* $\gamma_1$, *cyan;* $\gamma_2$, *orange), onto the critical manifold. The dashed line with double arrows represents a stimulus: * represents the first stimulus and ** the second.* (b) *Projection into the* $(x, V)$*-plane (with inset close-up of the funnel).*

Figure 11 shows the solution from Figure 8(e) projected into both $(f, x, V)$ and $(x, V)$ phase spaces. In Figure 11(a) we have again superimposed the complete $1^2 1^0$ solution (brown), along with the three leading maximal canards ($\gamma_0$, magenta; $\gamma_1$, cyan; $\gamma_2$, orange) and the partitioned curve of approach, onto the critical manifold in $(f, x, V)$ phase space. Similarly to the case of pulse-induced termination of EADs, the stimulus occurs while the trajectory is within the segment of the curve of approach with cardinality of 2. However, unlike in the previous case, the PCL is large enough for the solution to complete two EADs before returning to the bottom sheet. The second pulse occurs before the solution can reach the curve of approach. As such, the solution is ejected (upward arrow, **) back to the upper sheet outside of the funnel region, resulting in an AP without EADs. Lacking EADs, this second AP repolarizes rapidly and a sufficiently long PCL allows the solution to slowly return to the cardinality 2 segment of the curve of approach, completing the cycle.

**5.4. Bistability creates the potential for hysteresis.** We have seen from Figures 10 and 11 that the novel behavior generated by pacing the Luo–Rudy I model cell is due to the complex interplay between the canards, the PCL, and the slow flow along the curve of approach. The production of regions of bistability between different EAD attractors in the periodically stimulated system is no exception. Figures 8(b) and 8(c) show two different attractors at PCL = 820 ms, but what determines whether a PCL of 820 ms produces APs without EADs (Figure 8(b)) or with EADs that are prematurely truncated by ensuing stimuli (Figure 8(c))? We know that if the trajectory is within the $1^0$ (magenta) segment of the curve of approach

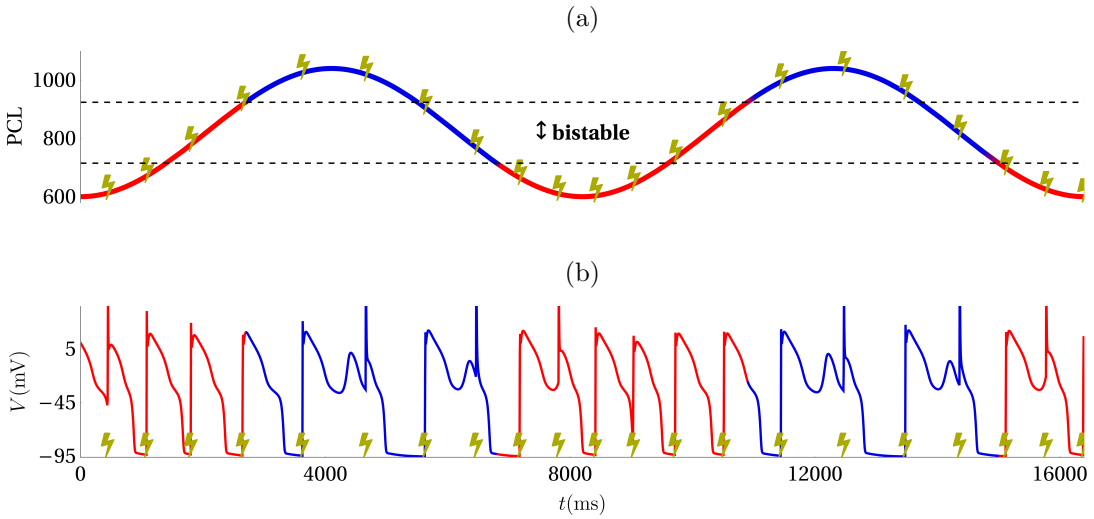


**Figure 12.** *Hysteresis is revealed by periodic variation of the PCL through a bistable interval.* (a) *Sinusoidal oscillations in the PCL across the bistable interval are imposed to induce switching behavior between the no EAD (red) and EAD (blue) attractors.* (b) *The voltage trace shows that for the same PCL value a standard AP can be produced or an AP with EADs, depending on whether the PCL is increasing (red) or decreasing (blue) through the bistable interval. The bistable interval is the horizontal band delimited by dashed lines in the upper panel. Lightning bolts (ϟ) in both panels denote the times at which pulses are applied.*

when a stimulus occurs, then an AP without EADs is produced. If the trajectory has not yet reached this segment when a stimulus is applied, then again an AP without EADs is produced. Hence, if the first stimulus occurs when the trajectory is in the $1^0$ segment or has not yet reached it, then standard APs will be produced. However, if the trajectory is in a different segment when the first stimulus occurs, then EADs that exhibit pulse-induced termination ($1^{1+}$) will occur.

A similar approach can be used to determine which pattern is produced in the second bistable interval. In this case, for example, with PCL = 1600 ms, if the phase point is in the $1^1$ segment of the curve of approach when the first stimulus is given, then periodic $1^1$ behavior will occur. If the phase point is in either the $1^0$ or $1^2$ segment, then a $1^21^0$ pattern will be produced. This is because if the phase point is in the $1^0$ segment during the first stimulus, then the resulting short AP will allow the trajectory to reach the $1^2$ segment before the next stimulus occurs. With the resulting long AP with two EADs, the trajectory will only reach the $1^0$ segment before the next stimulus arrives, restarting the $1^21^0$ cycle.

The bistability that is present over two PCL intervals provides the foundation for hysteresis in the system for slowly varying PCLs. We demonstrate this in Figure 12 for the cases of a periodically varying PCL that covers one of the bistable intervals. The traces in both panels are partitioned into red or blue segments in accordance with the coloring used in Figure 8(a); red segments denote that the trajectory is in the basin of attraction of APs with no EADs according to the location of the stimulus on the curve of approach (e.g., the $1^0$ segment), while blue segments denote that the trajectory is in the basin for APs with EADs (i.e., the

$1^{1+}$ segment). The red segments of the time course begin when the PCL decreases below 715 ms—the value at which the blue solution family loses stability and the red branch is the only attractor. The blue segments begin when the PCL increases above 924 ms—the PCL at which the red solution family loses stability and the blue branch is the only attractor. The bistable region, between these two critical PCL values, is shown as a horizontal strip delimited by dashed lines in Figure 12(a). In both panels, the times at which pulses are applied are labeled with lightning bolts (ϟ).

While hysteresis is not a novel behavior, it does have important implications. In particular, within a bistable interval, the existence of EADs depends not just on the PCL, but also on prior values of the PCL. For example, if the PCL is slowly increased through the bistable interval (red curves in Figure 12(a)), then the PCL threshold for EAD generation is higher ($>$ 900 ms) than it is if the PCL is slowly decreased through the bistable interval ($\approx$ 700 ms, blue curves). This could influence the interpretation of experimental studies in which the EAD threshold is determined by varying the PCL.

**6. Discussion.** Recent mathematical studies of a minimal model for the electrical activity of cardiomyocytes demonstrated that canards organize the emergence and properties of EADs [23] and that the finding that EADs occur only at long PCLs can be explained in terms of canards [45]. The current study extends this prior work by using a more biophysical model. With this model, we demonstrated that large EADs can be produced as a result of canards, and that these EADs occur far in phase space from the folded node singularity that gives rise to the canards. This is unlike prior results with the minimal model, where the EADs are found near the folded node and can be explained by singular limit analysis [23, 45]. Although the model that we used has a higher dimension, which makes the analysis more difficult, it has additional benefits beyond the larger EAD amplitude. In particular, behaviors that have been observed experimentally, such as alternans that pair APs with and without EADs [1, 3, 29, 35] and APs with aborted EADs [1, 10, 29], are produced by the higher-dimensional model, and can be understood in terms of canards.

Hypokalemia is a reliable condition for inducing EADs in cardiomyocytes [25, 30, 31, 49]. This condition, achieved by decreasing the extracellular $K^+$ concentration, increases the magnitude of the $K^+$ Nernst potential. This effect is replicated in Figure 3. At larger values of the extracellular $K^+$ concentration it is unlikely to see EADs, while at lower values the likelihood of EAD production is much greater. Why is this? Twists in the top sheet of the slow manifold are present throughout the range of values of $[K^+]_o$, but for larger $[K^+]_o$ values the trajectory does not enter the funnel following a stimulus, so it experiences no twists. Smaller values of $[K^+]_o$ move the twisted region closer to the location in phase space that the trajectory enters following a stimulus, making it more likely that EADs will be produced.

Figure 3 also indicates that increasing the $Ca^{2+}$ conductance, $g_{Ca}$, is a maneuver that can convert an AP to an AP with EADs. How does this happen? Again, this occurs because increasing $g_{Ca}$ moves the twisted region of the slow manifold closer to where the trajectory is injected upon stimulation. This can explain the experimental finding that exposing myocytes to BayK8644, a drug that increases $Ca^{2+}$ current, can induce EADs [35]. In the model, if $g_{Ca}$ is increased too much then the equilibrium $E_2$ stabilizes, so that following stimulation the trajectory does not repolarize to the rest state (at $E_1$). This is the reason that the EAD region

is so narrow in Figure 3 at higher values of $[K^+]_o$; the large values of $g_{Ca}$ needed to move the twists sufficiently close to the injection site to induce EADs are nearly large enough to stabilize $E_2$. So even a small additional increase in $g_{Ca}$ will be sufficient to induce depolarization block (and no repolarization).

This discussion shows the advantage of knowing the slow-fast structure of the system. Computer simulations, as were done to construct Figure 3, can indicate what behaviors occur across parameter space, but not why they occur. The slow-fast analysis tells us why, and thereby provides the means to interpret both computational and experimental findings.

Our slow-fast approach to the problem is similar in some ways to a previous mathematical analysis of EADs in a modified 4D Luo–Rudy I model that used a (1,3)–slow-fast decomposition [43]. Contrary to this previous analysis, our work utilized an alternative (2,2)–slow-fast decomposition that did not require alteration of the model's intrinsic timescale structure. Our approach revealed that canards induced by a folded node singularity were a possible explanation for EADs, but that the EADs occur far from where the singular analysis predicts that they should (Figure 4). Figure 5 shows how increasing the capacitance dramatically shifts twists in the slow manifold away from the folded node, and this is accompanied by a shift in the funnel (Figure 6). Importantly, along with the shift in location, the size of the twists increased significantly, resulting in EADs of an amplitude that is similar to those often seen in experiments (e.g., [28, 51]). Such large EADs were not produced by the minimal model studied previously [23, 45].

Another property of this model under pacing that was not seen in the minimal model is bistability (Figure 8). This leads naturally to hysteresis for slow variation of the PCL across a bistable interval (Figure 12). To our knowledge, such bistability or hysteresis has not been reported in experimental studies of EADs, but it is also unlikely that either was explicitly investigated. Bistability could be investigated with a fixed PCL, in a bistable interval, and the application of occasional additional stimuli to perturb the trajectory from one basin of attraction to another. The hysteresis effect could be observed by slowly ramping the PCL up and then slowly ramping it down (or vice versa) over the bistable interval. We have not seen studies employing either protocol, so such behaviors qualify as untested model predictions.

A potential limitation of using this model is that it only allows for the production of EADs through a strictly electrical process. However, there is experimental evidence that spontaneous release of $Ca^{2+}$ from the sarcoplasmic reticulum is an alternate mechanism for EADs [19, 20]. A model demonstrating how this could work was recently published [50]. An additional limitation of this model is that it does not include some ionic currents that have been shown to play a role in EAD genesis. These additional currents include, for instance, late $Na^+$ ($I_{Na,L}$) [14] and the $Na^+$-$Ca^{2+}$ exchanger ($I_{NCX}$) [40].

These myriad routes to EAD genesis raise important questions about the ubiquity of the canard mechanism. For example, does the intracellular $Ca^{2+}$-handling subsystem possess the elements necessary for canard dynamics? Or, does the canard mechanism, as it has been shown to underlie voltage-driven EADs, persist under the added complexity brought on by other ionic currents? It may be the case that from a dynamics viewpoint the mechanism is the same, even though the biological substrate for the dynamics differs substantially. Indeed, the hormone-secreting endocrine cells of the pituitary gland produce bursting electrical activity that appears quite similar to APs with EADs, although the bursts are much longer [41]. The

dynamical mechanism of these bursts has been suggested to be canards induced by a folded node singularity, just as we suggest for EADs [46]. Thus, it seems possible that the dynamic phenomenon may appear in different contexts and using different biological substrates, but the common element is twisting of slow manifolds and the canard solutions that accompany this twisting.

**Appendix A. The modified Luo–Rudy I model.** We describe here the model used throughout the study. This includes formulations for each of the ionic currents, the gating expressions, and time constants as well as a table of parameter values.

The model differential equations are

$$\begin{aligned} C_m \frac{\mathrm{d}V}{\mathrm{d}t} &= -(I_{\mathrm{Ca}} + I_{\mathrm{K}} + I_{\mathrm{K1}} + I_{\mathrm{Kp}} + I_{\mathrm{b}}) + I_{\mathrm{stim}}, \\ \frac{\mathrm{d}d}{\mathrm{d}t} &= \frac{d_\infty(V) - d}{\tau_d(V)}, \\ \frac{\mathrm{d}f}{\mathrm{d}t} &= \frac{f_\infty(V) - f}{\tau_f(V)}, \\ \frac{\mathrm{d}x}{\mathrm{d}t} &= \frac{x_\infty(V) - x}{\tau_x(V)} \end{aligned}$$

with ionic currents given by

$$\begin{aligned} I_{\mathrm{Ca}} &= g_{\mathrm{Ca}}\, d\, f\, (V - V_{\mathrm{Ca}}), \\ I_{\mathrm{K}} &= g_{\mathrm{K}}\, x\, \mathrm{X}_{\mathrm{i},\infty}(V)\, (V - V_{\mathrm{K}}), \\ I_{\mathrm{K1}} &= g_{\mathrm{K1}}\, \mathrm{K}_{1,\infty}(V)\, (V - V_{\mathrm{K1}}), \\ I_{\mathrm{Kp}} &= g_{\mathrm{Kp}}\, \mathrm{K}_{\mathrm{p},\infty}(V)\, (V - V_{\mathrm{Kp}}), \\ I_{\mathrm{b}} &= g_{\mathrm{b}}\, (V - V_{\mathrm{b}}), \end{aligned}$$

where

$$y_\infty(V) = \frac{\alpha_y(V)}{\alpha_y(V) + \beta_y(V)} \quad \text{and} \quad \tau_y(V) = \frac{1}{\alpha_y(V) + \beta_y(V)} \quad \text{for} \quad y = d, f, x, \text{ and } \mathrm{K}_1.$$

Separate tables for the voltage-dependent rate constants/instantaneous gating expressions and the parameter values used in the analysis are presented below. Table 1 includes both the voltage-dependent rate constants, $\alpha_y$ and $\beta_y$, for each of the gating variables $d, f$, and $x$ and the instantaneous gating expressions for inactivation of $I_{\mathrm{K}}$ and activation of $I_{\mathrm{Kp}}$. Table 2 gives the parameter values used in our analysis. The value of the parameter $T$ that appears in the Nernst equations for $V_{\mathrm{K}}$ and $V_{\mathrm{K1}}$ was reduced from the original value used in [27] (310.15 K) in order to obtain the same Nernst potential, $V_{\mathrm{K}} = -77$ mV, used in [43].

**Appendix B. Computation of the EAD onset boundary.** The EAD onset boundary was computed by continuation of a particular solution to a suitably posed 2-point boundary value problem. Formulation of the problem relies on the fact that the emergence of EADs should correspond to a bifurcation of standard AP solutions due to increases in the parameter, $g_{\mathrm{Ca}}$. However, the system under consideration is nonautonomous, requiring time-dependent

**Table 1**

| | |
|---|---|
| Voltage-dependent rate constants | |
| $\boldsymbol{d}$: | $\alpha_d(V) = 0.095\dfrac{e^{-0.01(V-5)}}{1+e^{-0.072(V-5)}}$ $\quad$ $\beta_d(V) = .07\dfrac{e^{-0.017(V+44)}}{1+e^{0.05(V+44)}}$ |
| $\boldsymbol{f}$: | $\alpha_f(V) = 0.012\dfrac{e^{-0.008(V+28)}}{1+e^{0.15(V+28)}}$ $\quad$ $\beta_f(V) = 0.0065\dfrac{e^{-0.02(V+30)}}{1+e^{-0.2(V+30)}}$ |
| $\boldsymbol{x}$: | $\alpha_x(V) = 0.0005\dfrac{e^{0.083(V+50)}}{1+e^{0.057(V+50)}}$ $\quad$ $\beta_x(V) = 0.0013\dfrac{e^{-0.06(V+20)}}{1+e^{-0.04(V+20)}}$ |
| Instantaneous gating expressions | |
| $\mathbf{K_1}$: | $\alpha_{K_1}(V) = \dfrac{1.02}{1+e^{0.2385(V-V_{K1}-59.215)}}$ <br> $\beta_{K_1}(V) = \dfrac{0.49124e^{0.08032(V-V_{K1}+5.476)} + e^{0.06175(V-V_{K1}-594.31)}}{1+e^{-0.5143(V-V_{K1}+4.753)}}$ |
| $\mathbf{X_i}$: | $X_{i,\infty}(V) = 2.837\dfrac{e^{0.04(V+77)}-1}{(V+77)e^{0.04(V+35)}}$ |
| $\mathbf{K_p}$: | $K_{p,\infty}(V) = \dfrac{1}{1+e^{-(V-7.488)/5.98}}$ |

**Table 2**

| |
|---|
| Ideal gas constants |
| $R = 8.3144598$ J/mol·K $\quad$ $T = 307.69146$ K $\quad$ $F = 96.4853329$ kC/mol |
| Ion concentrations |
| $[K^+]_o = 5.4$ mM (default), 3.0 mM (EADs) $\quad$ $[K^+]_i = 145$ mM <br> $[Na^+]_o = 140$ mM $\quad$ $[Na^+]_i = 18$ mM <br> PRNaK ($Na^+$ permeability of $I_K$ channels) = 0.01833 |
| Maximal conductances |
| $g_{Ca} = 0.09$ mS/cm$^2$ (default), 0.123 mS/cm$^2$ (EADs) $\quad$ $g_K = 0.282\sqrt{[K^+]_o/5.4\text{ mM}}$ mS/cm$^2$ <br> $g_{K1} = 0.6047\sqrt{[K^+]_o/5.4\text{ mM}}$ mS/cm$^2$ $\quad$ $g_{Kp} = 0.0183$ mS/cm$^2$ $\quad$ $g_b = 0.03921$ mS/cm$^2$ |
| Nernst potentials |
| $V_{Ca} = 80.0$ mV $\quad$ $V_K = \dfrac{RT}{F}\text{Log}\left(\dfrac{[K^+]_o + \text{PRNaK}[Na^+]_o}{[K^+]_i + \text{PRNaK}[Na^+]_i}\right) = -76.994$ mV <br> $V_{K1} = \dfrac{RT}{F}\text{Log}\left(\dfrac{[K^+]_o}{[K^+]_i}\right) = -87.2425$ mV $\quad$ $V_{Kp} = V_{K1}$ $\quad$ $V_b = 59.87$ mV |

forcing in order to exhibit APs. To obtain an extended autonomous analogue, we introduce $s$ as a dummy variable that parameterizes time (i.e., $\dot{s} = 1$ with $s(0) = 0$) and for smoothness/numerical feasibility, we approximate the (single) square-wave pulse current as

$$I_{\text{stim}}(s) = \frac{a}{2}\left[\tanh\left(\frac{s-1}{\sigma}\right) - \tanh\left(\frac{s-3}{\sigma}\right)\right], \tag{B.1}$$

where $a = 70\ \mu\text{A/cm}^2$ is the maximum amplitude of the square wave and $\sigma = 20$ sets its steepness. This expression gives a single pulse that initiates at $s \approx 1$ ms and terminates at $s \approx 3$ ms.

A starting solution, without EADs, is generated by numerical integration of the autonomous extended initial value problem. To do this, we simply choose parameter values that lie within the region of parameter space where EADs are absent (green in Figure 3). This solution is initialized at the hyperpolarized equilibrium, $E_1$ (which is globally stable in the absence of forcing), and is halted when voltage reaches a chosen value, $V_{\text{rep}} = -70$ mV, that indicates repolarization. Our particular starting solution was computed using the default parameter values, $g_{\text{Ca}} = 0.09\ \text{mS/cm}^2$ and $[\text{K}^+]_{\text{o}} = 5.4$ mM.

This general setup can be represented formally as a 2-point boundary value problem:

$$\dot{\mathbf{u}} = T\,\boldsymbol{g}(\mathbf{u}, \mathbf{p}), \quad \mathbf{u} = \begin{pmatrix} V \\ d \\ f \\ x \\ s \end{pmatrix}, \quad \mathbf{p} = \begin{pmatrix} g_{Ca} \\ [\text{K}^+]_o \end{pmatrix}, \tag{B.2}$$

$$\begin{pmatrix} V(0) \\ d(0) \\ f(0) \\ x(0) \end{pmatrix} = \begin{pmatrix} V_{E_1} \\ d_{E_1} \\ f_{E_1} \\ x_{E_1} \end{pmatrix}, \quad \begin{pmatrix} V(1) \\ s(1) \end{pmatrix} = \begin{pmatrix} V_{\text{rep}} \\ T \end{pmatrix}. \tag{B.3}$$

Here, $T$ is the total integration time, scaling the time domain so that $t \in [0, 1]$, and $\boldsymbol{g}(\cdot, \cdot)$ is the extended vector field. Having 6 boundary conditions (4 at $t = 0$ and 2 at $t = 1$) allows us to continue the starting solution in two parameters; we choose $(g_{\text{Ca}}, T)$ since increases in $g_{\text{Ca}}$ generically lead to EADs for fixed $[\text{K}^+]_{\text{o}}$. With respect to Figure 3, continuing in both $g_{\text{Ca}}$ and $T$ lets us traverse the grid rightward, toward the suspected EAD boundary, while letting the total integration time grow with the extended duration of APs. The EAD boundary is marked by a heteroclinic bifurcation connecting equilibria $E_1$ and $E_3$. The depolarized segment of this heteroclinic orbit coincides with the primary strong canard $\gamma_0$. Once located, this heteroclinic orbit can be continued in the three system parameters $(g_{\text{Ca}}, [\text{K}^+]_{\text{o}}, T)$ in order to generate the EAD initiation curve.

**Appendix C. Dimensional analysis and limiting subproblems.** To show that the Luo–Rudy I model is a multitimescale system, we begin by rescaling each of the time constants $\tau_j(V) = \bar{\tau}_j \cdot \tilde{\tau}_j(V)$ for $j = d, f, x$, where each $\bar{\tau}_j$ is the average time constant attained over the duration of the AP with 2 EADs (from stimulus initiation until 90% repolarization) depicted in Figure 2(d). Next, we nondimensionalize the system via the rescalings

$$V = k_v v, \quad t = k_t t_s, \quad g_x = G_{\text{tot}} \bar{g}_x, \quad x \in \{\text{Ca}, \text{K}, \text{K1}, \text{Kp}, \text{b}\}, \tag{C.1}$$

where $k_v = 100$ mV and $k_t = \bar{\tau}_f = 173$ ms are reference voltage and timescales, respectively, $G_{\text{tot}} = 0.841$ mS/cm$^2$ is the sum of all conductances, and $\overline{g}_x$ denotes the dimensionless conductances. With these rescalings, the dimensionless version of (2.1) is

$$\begin{aligned}
\epsilon \frac{\mathrm{d}v}{\mathrm{d}t_s} &= -(\overline{I}_{\text{Ca}} + \overline{I}_{\text{K}} + \overline{I}_{\text{K1}} + \overline{I}_{\text{Kp}} + \overline{I}_{\text{b}}) =: F_1(v, d, f, x),\\
\frac{\epsilon}{r}\frac{\mathrm{d}d}{\mathrm{d}t_s} &= \frac{d_\infty(v) - d}{\tilde{\tau}_d(v)} =: F_2(v, d),\\
\frac{\mathrm{d}f}{\mathrm{d}t_s} &= \frac{f_\infty(v) - f}{\tilde{\tau}_f(v)} =: H_1(v, f),\\
\frac{\mathrm{d}x}{\mathrm{d}t_s} &= \frac{\bar{\tau}_f}{\bar{\tau}_x}\frac{x_\infty(v) - x}{\tilde{\tau}_x(v)} =: H_2(v, x),
\end{aligned} \tag{C.2}$$

where $\epsilon := \frac{C_m/G_{\text{tot}}}{\bar{\tau}_f} \approx 0.007$ and $r := \frac{C_m/G_{\text{tot}}}{\bar{\tau}_d} \approx 0.05$ (as in the main text), and each of $F_1, F_2, H_1$, and $H_2$ are $\mathcal{O}(1)$. The system (C.2) is identical to (3.1) aside from ascribing shorthand labels to each of the expressions of the right-hand side.

As written, system (C.2) describes the evolution of Luo–Rudy I on the slow timescale. By rescaling time, $t_f = \frac{t_s}{\epsilon}$, we can rewrite the system in reference to the fastest timescale:

$$\begin{aligned}
\frac{\mathrm{d}v}{\mathrm{d}t_f} &= F_1(v, d, f, x),\\
\frac{\mathrm{d}d}{\mathrm{d}t_f} &= rF_2(v, d),\\
\frac{\mathrm{d}f}{\mathrm{d}t_f} &= \epsilon H_1(v, f),\\
\frac{\mathrm{d}x}{\mathrm{d}t_f} &= \epsilon H_2(v, x).
\end{aligned} \tag{C.3}$$

Systems (C.2) and (C.3) are equivalent in that their solutions trace out the same paths in the $(v, d, f, x)$ phase space; the different time parameterizations determine the rate at which solutions move in phase space.

We can then take advantage of the intrinsic separation in timescales to formally decompose (C.2) into the constituent fast and slow subsystems ((3.2) and (3.3), respectively) that appear in the main text. Taking the limit $\epsilon \to 0$ in (C.3) gives the fast subsystem

$$\begin{aligned}
\frac{\mathrm{d}V}{\mathrm{d}t_f} &= F_1(v, d, f, x),\\
\frac{\mathrm{d}d}{\mathrm{d}t_f} &= r\, F_2(v, d),\\
\frac{\mathrm{d}f}{\mathrm{d}t_f} &= 0,\\
\frac{\mathrm{d}x}{\mathrm{d}t_f} &= 0,
\end{aligned} \tag{C.4}$$

and taking the singular limit, $\epsilon \to 0$, of (C.2) yields the slow subsystem

$$\begin{aligned} 0 &= F_1(v,d,f,x), \\ 0 &= F_2(v,d), \\ \frac{\mathrm{d}f}{\mathrm{d}t_s} &= H_1(v,f), \\ \frac{\mathrm{d}x}{\mathrm{d}t_s} &= H_2(v,x). \end{aligned} \tag{C.5}$$

While (C.2) and (C.3) are equivalent up to the rate at which solutions evolve in phase space, the corresponding limiting subproblems (C.4) and (C.5) are not.

**Appendix D. Bifurcations of the fast subsystem.** Here we give a more detailed treatment of the bifurcation structure of the fast subsystem. The set of equilibria of the fast subsystem,

$$S := \{(v,d,f,x) \in \mathbb{R}^4 : F_1(v,d,f,x) = F_2(v,d) = 0\}, \tag{D.1}$$

is called the critical manifold and can be represented globally as the graph over $(v,x)$ given by (3.4). The critical manifold is cubic shaped (Figure 4), with upper and lower attracting sheets, $S_0^{a,+}$ and $S_0^{a,-}$ (Figure 4(a), blue surfaces), and a middle sheet, $S_0^s$ (Figure 4(a), red surface), of saddle-type. The $S_0^{a,+}$ and $S_0^s$ sheets are separated by a 1D curve (Figure 4, green), $L$, of fold bifurcations of (3.2):

$$L := \left\{ (v,d,f,x) \in S : \det \boldsymbol{J}_r = r\left(\frac{\partial F_1}{\partial v}\frac{\partial F_2}{\partial d} - \frac{\partial F_1}{\partial d}\frac{\partial F_2}{\partial v}\right) = 0 \right\}, \tag{D.2}$$

where

$$\boldsymbol{J}_r = \begin{pmatrix} \frac{\partial F_1}{\partial v} & \frac{\partial F_1}{\partial d} \\ r\frac{\partial F_2}{\partial v} & r\frac{\partial F_2}{\partial d} \end{pmatrix}$$

is the Jacobian of the fast subsystem. The saddle and lower attracting sheets are also separated by another 1D fold curve, but this curve falls far outside of the physiologically meaningful phase space and does not play any role in model dynamics. Here, and for the remainder of the appendix, we suppress the explicit dependence of the right-hand side expressions on the dynamical (dimensionless) variables.

Since the fast subsystem is planar, Hopf bifurcations and emerging periodic solutions of the fast subsystem are possible, and it has been suggested that these are responsible for EADs in the Luo–Rudy 1 model [43]. Necessary conditions for the existence of a 1D curve of Hopf bifurcations are given by

$$H := \left\{ (v,d,f,x) \in S : \det \boldsymbol{J}_r > 0 \text{ and } \operatorname{tr} \boldsymbol{J}_r = \frac{\partial F_1}{\partial v} + r\frac{\partial F_2}{\partial d} = 0 \right\}. \tag{D.3}$$

However, for physiologically meaningful regions of parameter space, phase space, and reasonable choices of $r$, the Hopf criteria (D.3) are never satisfied.

**Appendix E. The slow subsystem, desingularization, and the folded node.** The slow subsystem assumes that the fast-$(v,\, d)$ dynamics adjust instantaneously to the slow motions

in $(f,\, x)$. The algebraic constraints of (3.3) then constrain the reduced flow to lie along the critical manifold. This makes the critical manifold the interface between the fast and slow subsystems.

The differential equations in system (3.3) describe the slow $(f, x)$ motions along $S$. To obtain a description of the $(v, d)$ motions slaved to $S$, we use the graph representation (3.4). Having a critical manifold with a global graph representation saves us from having to analyze the reduced flow under a suitable atlas of coordinate charts. Hence, we can reobtain globally valid explicit expressions for the motions of the fast variables and project onto the $(v,\, x)$-plane. More specifically, we take a total time derivative of the algebraic constraints in (3.3) and rearrange to obtain

$$\begin{pmatrix} -\boldsymbol{J} & \mathbf{0} \\ \mathbf{0} & \boldsymbol{I}_2 \end{pmatrix} \frac{\mathrm{d}}{\mathrm{d}t_s} \begin{pmatrix} v \\ d \\ f \\ x \end{pmatrix} = \begin{pmatrix} \dfrac{\partial F_1}{\partial f} H_1 + \dfrac{\partial F_1}{\partial x} H_2 \\ 0 \\ H_1 \\ H_2, \end{pmatrix}, \tag{E.1}$$

where

$$\boldsymbol{J} = \begin{pmatrix} \frac{\partial F_1}{\partial v} & \frac{\partial F_1}{\partial d} \\ \frac{\partial F_2}{\partial v} & \frac{\partial F_2}{\partial d} \end{pmatrix},$$

$\boldsymbol{I}_2$ is the $2 \times 2$ identity matrix, and $\mathbf{0}$ is the $2 \times 2$ zero matrix. We then left-multiply both sides of the equation by the matrix $\left(\begin{smallmatrix} -\mathrm{adj}\ \boldsymbol{J} & \mathbf{0} \\ \mathbf{0} & \boldsymbol{I}_2 \end{smallmatrix}\right)$, where adj $\boldsymbol{J}$ is the adjoint (or adjugate) of $\boldsymbol{J}$, to obtain:

$$\begin{pmatrix} (\det\, \boldsymbol{J})\, \boldsymbol{I}_2 & \mathbf{0} \\ \mathbf{0} & \boldsymbol{I}_2 \end{pmatrix} \frac{\mathrm{d}}{\mathrm{d}t_s} \begin{pmatrix} v \\ d \\ f \\ x \end{pmatrix} = \begin{pmatrix} -\frac{\partial F_2}{\partial d} \left( \frac{\partial F_1}{\partial f} H_1 + \frac{\partial F_1}{\partial x} H_2 \right) \\ \frac{\partial F_2}{\partial v} \left( \frac{\partial F_1}{\partial f} H_1 + \frac{\partial F_1}{\partial x} H_2 \right) \\ H_1 \\ H_2 \end{pmatrix}. \tag{E.2}$$

In light of (3.4) (with $V$ rescaled), the differential equations for the evolution of $d$ and $f$ in (E.2) are redundant. As such, the remaining 2D $(v,\, x)$ system is

$$\begin{aligned} (\det\, \boldsymbol{J})\, \frac{\mathrm{d}v}{\mathrm{d}t_s} &= -\frac{\partial F_2}{\partial d} \left( \frac{\partial F_1}{\partial f} H_1 + \frac{\partial F_1}{\partial x} H_2 \right), \\ \frac{\mathrm{d}x}{\mathrm{d}t_s} &= H_2, \end{aligned} \tag{E.3}$$

where $d$ and $f$ are given by (3.4) (rescaled).

System (E.3) is equivalent to the original reduced system (3.3); it is the projection onto the $(v, x)$-plane. More importantly, the projection (E.3) highlights that the reduced flow experiences a finite-time blowup of solutions in the regions of phase space where $\det \boldsymbol{J} = 0$, exactly at the fold curves. To handle this finite-time blowup of solutions, we make the phase-

space-dependent time rescaling $dt_s = (\det \boldsymbol{J})\, dt_d$, which gives the *desingularized system*

$$\begin{aligned} \frac{\mathrm{d}v}{\mathrm{d}t_d} &= -\frac{\partial F_2}{\partial d}\left(\frac{\partial F_1}{\partial f} H_1 + \frac{\partial F_1}{\partial x} H_2\right) := Y(v,x), \\ \frac{\mathrm{d}x}{\mathrm{d}t_d} &= (\det \boldsymbol{J})\, H_2. \end{aligned} \tag{E.4}$$

The benefit of this transformation is that the fold curves, $L^{\pm}$, have been converted from singularities of the reduced problem (E.3) into nullclines of the desingularized system (E.4). Thus, we study the desingularized system in order to learn about the dynamics of the reduced system. Care must be taken, however, in relating systems (E.3) and (E.4). The phase-space-dependent time rescaling reverses the direction of flow on the middle sheet of saddle-type (where $\det \boldsymbol{J} < 0$) and may introduce additional equilibria beyond those present in (3.3) or (3.1), which do not correspond to true equilibria of the full flow.

Any additional equilibria of (E.4) that are introduced by the desingularization must lie along folds, satisfying

$$E_{FS} := \{(V, d, f, x) \in L : Y = 0\}. \tag{E.5}$$

These special points of (E.4), called *folded singularities*, are the same points of (E.3) where a cancellation of simple zeroes in a l'Hôpital-type limit occurs. That is, solutions of (E.3) can cross the fold with finite speed at these points (where uniqueness of solutions is lost). These solutions are called singular canards.

Stable nodes within a fold of (E.4), called folded node singularities, have been shown to organize the small oscillations of mixed-mode dynamics, including those of EADs. We find that the desingularized reduced system possesses a folded node singularity ($FN$, purple), shown on the fold curve, $L$, in Figure 4. Along with the folded node comes a submanifold of $S_0^{a,+}$ called the singular funnel which funnels all entrant solutions through the folded node. The funnel is bounded from below by the upper fold curve, $L$, and from above by the strong stable manifold of the folded node. The strong stable manifold (tangent to the dominant eigenvector) of the folded node is called the strong singular canard, and is depicted in Figure 4 ($\gamma_0$; purple). Similarly, the weak stable manifold (tangent to the nondominant eigenvector) of the folded node is called the weak singular canard (not depicted).

## Appendix F. The stability properties of the equilibrium $E_2$ under variation in $C_m$.

In contrast with canonical geometric singular perturbation analysis, where the qualitative stability properties of ordinary singularities are preserved away from the singular limit, the singularity $E_2$ in our system is a saddle point under the singular limit (i.e., $E_2$ is on $S_0^s$ in Figure 4) but, undergoes a subcritical Hopf bifurcation to gain stability as $C_m$ approaches the default value 1 $\mu$F/cm$^2$ in the full system. Equilibrium $E_2$ is the only one for which a change in stability occurs between the singular and nonsingular problems. Figure 13 shows how the real parts of the eigenvalues of $E_2$ vary under changes in $C_m$.

Starting near $C_m \approx 0$ $\mu$F/cm$^2$, $E_2$ is a saddle point with 4 real eigenvalues: 2 ($\lambda_{1,2}$: dashed black and red curves, respectively) are positive and 2 ($\lambda_{3,4}$: solid green and blue curves, respectively) are negative. Near $C_m \approx 0.2$ $\mu$F/cm$^2$, the two positive eigenvalues coalesce along

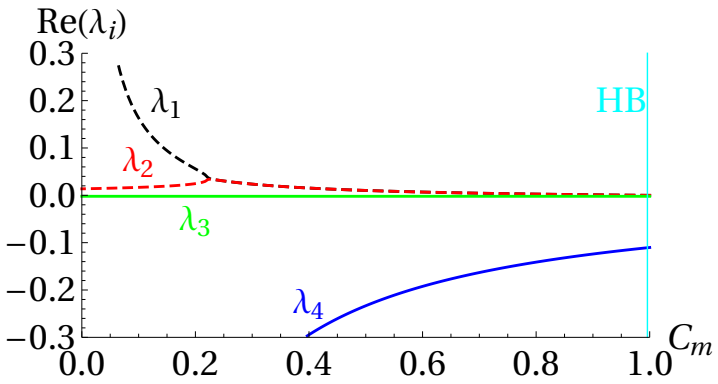


**Figure 13.** *Real parts of the eigenvalues of* $\boldsymbol{E_2}$ *for* $g_{Ca} = 0.123$ $mS/cm^2$ *and* $[K^+]_o = 3.0$ $mM$.

the real axis and become a complex conjugate pair, with positive real part. This configuration of eigenvalues remains through further increases in $C_m$, until the subcritical Hopf bifurcation point (HB, vertical cyan segment), near $C_m \approx 0.996$ $\mu$F/cm$^2$, is reached and $\lambda_{1,2}$ cross the imaginary axis, making $E_2$ stable.

## REFERENCES


[1] A. Bapat, T. P. Nguyen, J.-H. Lee, A. A. Sovari, M. C. Fishbein, J. N. Weiss, and H. S. Karagueuzian, *Enhanced sensitivity of aged fibrotic hearts to angiotensin II- and hypokalemia-induced early afterdepolarization-mediated ventricular arrhythmias*, Amer. J. Physiol., 302 (2012), pp. H2331–H2340, https://doi.org/10.1152/ajpheart.00094.2012.

[2] H. Cserne Szappanos, H. Viola, and L. C. Hool, *L-type calcium channel: Clarifying the oxygen sensing hypothesis*, Int. J. Biochem. Cell B., 86 (2017), pp. 32–36, https://doi.org/10.1016/j.biocel.2017.03.010.

[3] B. P. Damiano and M. R. Rosen, *Effects of pacing on triggered activity induced by early afterdepolarizations*, Circulation, 69 (1984), pp. 1013–1025, https://doi.org/10.1161/01.CIR.69.5.1013.

[4] J. M. Davidenko, L. Cohen, R. Goodrow, and C. Antzelevitch, *Quinidine-induced action potential prolongation, early afterdepolarizations, and triggered activity in canine Purkinje fibers. Effects of stimulation rate, potassium, and magnesium*, Circulation, 79 (1989), pp. 674–686.

[5] M. Desroches, J. Guckenheimer, B. Krauskopf, C. Kuehn, H. M. Osinga, and M. Wechselberger, *Mixed-mode oscillations with multiple time scales*, SIAM Rev., 54 (2012), pp. 211–288, https://doi.org/10.1137/100791233.

[6] M. Desroches, B. Krauskopf, and H. M. Osinga, *The geometry of slow manifolds near a folded node*, SIAM J. Appl. Dyn. Syst., 7 (2008), pp. 1131–1162, https://doi.org/10.1137/070708810.

[7] E. J. Doedel, B. E. Oldeman, A. R. Champneys, F. Dercole, T. Fairgrieve, Y. Kuznetsov, R. Paffenroth, B. Sandstede, X. Wang, and C. Zhang, *AUTO-07P: Continuation and Bifurcation Software for Ordinary Differential Equations*, manuscript.

[8] N. Fenichel, *Geometric singular perturbation theory for ordinary differential equations*, J. Differential Equations, 31 (1979), pp. 53–98, https://doi.org/10.1016/0022-0396(79)90152-9.

[9] J. J. Fox, J. L. Mcharg, and R. F. Gilmour, *Ionic mechanism of electrical alternans*, Amer. J. Physiol., 282 (2002), pp. H516–H530.

[10] N. Gaur, Y. Rudy, and L. Hool, *Contributions of ion channel currents to ventricular action potential changes and induction of early afterdepolarizations during acute hypoxia*, Circ. Res., 105 (2009), pp. 1196–1203, https://doi.org/10.1161/CIRCRESAHA.109.202267.

[11] R. F. Gilmour and S. Moïse, *Triggered activity as a mechanism for inherited ventricular arrhythmias in German shepherd dogs*, J. Amer. Coll. Cardiol., 27 (1996), pp. 1526–1533, https://doi:10.1016/0735-1097(95)00618-4.

[12] C. R. Hasan, B. Krauskopf, and H. M. Osinga, *Saddle slow manifolds and canard orbits in $\mathbb{R}^4$ and application to the full Hodgkin-Huxley model*, J. Math. Neurosci., 8 (2018), 5, https://doi.org/10.1186/s13408-018-0060-1.

[13] A. L. Hodgkin and A. F. Huxley, *A quantitative description of membrane current and its application to conduction and excitation in nerve*, J. Physiol., 117 (1952), pp. 500–544, https://doi.org/10.1007/BF02459568.

[14] B. Horvath, T. Banyasz, Z. Jian, B. Hegyi, K. C. Kistamas, P. P. Nanasi, L. T. Izu, Y. Chen-Izu, and Y. Edu, *Dynamics of the Late $Na^+$ current during cardiac action potential and its contribution to afterdepolarizations*, J. Mol. Cell. Cardiol., 64 (2013), pp. 59–68, https://doi.org/10.1016/j.yjmcc.2013.08.010.

[15] C. T. January and J. M. Riddle, *Early afterdepolarizations: mechanism of induction and block. A role for L-type $Ca^{2+}$ current*, Circ. Res., 64 (1989), pp. 977–990, https://doi.org/10.1161/01.RES.64.5.977.

[16] C. K. R. T. Jones, *Geometric singular perturbation theory*, in Dynamical Systems, Springer, Berlin, 1995, pp. 44–118, https://doi.org/10.1007/BFb0095239.

[17] R. A. Josephson, H. S. Silverman, E. G. Lakatta, M. D. Stern, and J. L. Zweier, *Study of the mechanisms of hydrogen peroxide and hydroxyl free radical-induced cellular injury and calcium overload in cardiac myocytes*, J. Biol. Chem., 266 (1991), pp. 2354–2361.

[18] J. Keener and J. Sneyd, *Mathematical Physiology I: Cellular Physiology*, Interdiscip. Appl. Math. 8, 2nd ed., Springer, New York, 2009, https://doi.org/10.1007/978-0-387-75847-3.

[19] J. J. Kim, J. Němec, Q. Li, and G. Salama, *Synchronous systolic subcellular $Ca^{2+}$-elevations underlie ventricular arrhythmia in drug-induced long QT type* 2, Circ. Arrhythm. Electrophysiol., 8 (2015), pp. 703–712, https://doi.org/10.1161/CIRCEP.114.002214.

[20] J. J. Kim, J. Němec, R. Papp, R. Strongin, J. J. Abramson, and G. Salama, *Bradycardia alters $Ca^{2+}$ dynamics enhancing dispersion of repolarization and arrhythmia risk*, Amer. J. Physiol., 304 (2013), 6, https://doi.org/10.1152/AJPHEART.00787.2012.

[21] M. Krupa and P. Szmolyan, *Extending geometric singular perturbation theory to nonhyperbolic points—fold and canard points in two dimensions*, SIAM J. Math. Anal., 33 (2001), pp. 286–314, https://doi.org/10.1137/S0036141099360919.

[22] P. Kügler, *Early afterdepolarizations with growing amplitudes via delayed subcritical Hopf bifurcations and unstable manifolds of saddle foci in cardiac action potential dynamics*, PLoS ONE, 11 (2017), e0151178, https://doi.org/10.1371/journal.pone.0151178.

[23] P. Kügler, A. H. Erhardt, and M. A. K. Bulelzai, *Early afterdepolarizations in cardiac action potentials as mixed mode oscillations due to a folded node singularity*, PLoS ONE, 13 (2018), e0209498, https://doi.org/10.1371/journal.pone.0209498.

[24] Y. Kurata, K. Tsumoto, K. Hayashi, I. Hisatome, M. Tanida, Y. Kuda, and T. Shibamoto, *Dynamical mechanisms of phase-2 early afterdepolarizations in human ventricular myocytes: Insights from bifurcation analyses of two mathematical models*, Amer. J. Physiol., 312 (2017), pp. H106–H127.

[25] J. Kuusela, K. Larsson, D. Shah, C. Prajapati, and K. Aalto-Setälä, *Low extracellular potassium prolongs repolarization and evokes early afterdepolarization in human induced pluripotent stem cell-derived cardiomyocytes*, Biol. Open, 6 (2017), pp. 777–784, https://doi.org/10.1242/bio.024216.

[26] G.-X. Liu, B.-R. Choi, O. Ziv, W. Li, E. De Lange, Z. Qu, G. Koren, and G. Koren, *Differential conditions for early after-depolarizations and triggered activity in cardiomyocytes derived from transgenic LQT1 and LQT2 rabbits*, J. Physiol., 590 (2012), pp. 1171–1180, https://doi.org/10.1113/jphysiol.2011.218164.

[27] C. H. Luo and Y. Rudy, *A model of the ventricular cardiac action potential*, Circ. Res., 68 (1991), pp. 1501–1526, https://doi.org/10.1161/01.RES.68.6.1501.

[28] R. V. Madhvani, Y. Xie, A. Pantazis, A. Garfinkel, Z. Qu, J. N. Weiss, and R. Olcese, *Shaping a new $Ca^{2+}$ conductance to suppress early afterdepolarizations in cardiac myocytes*, J. Physiol., 589 (2011), pp. 6081–6092, https://doi.org/10.1113/jphysiol.2011.219600.

[29] T. P. Nguyen, Y. Xie, A. Garfinkel, Z. Qu, and J. N. Weiss, *Arrhythmogenic consequences of myofibroblast-myocyte coupling*, Cardiovasc. Res., 93 (2012), pp. 242–251, https://doi.org/10.1093/cvr/cvr292.

[30] O. E. Osadchii, *Mechanisms of hypokalemia-induced ventricular arrhythmogenicity*, Fund. Clin. Pharmacol., 24 (2010), pp. 547–559, https://doi.org/10.1111/j.1472-8206.2010.00835.x.

[31] A. Pezhouman, N. Singh, Z. Song, M. Nivala, A. Eskandari, H. Cao, A. Bapat, C. Y. Ko, T. P. Nguyen, Z. Qu, H. S. Karagueuzian, and J. N. Weiss, *Molecular basis of hypokalemia-induced ventricular fibrillation*, Circulation, 132 (2015), pp. 1528–1537, https://doi.org/10.1161/CIRCULATIONAHA.115.016217.

[32] Y. Prudat, R. V. Madhvani, M. Angelini, N. P. Borgstom, A. Garfinkel, H. S. Karagueuzian, J. N. Weiss, E. de Lange, R. Olcese, and J. P. Kucera, *Stochastic pacing reveals the propensity to cardiac action potential alternans and uncovers its underlying dynamics*, J. Physiol., 594 (2016), pp. 2537–2553, https://doi.org/10.1113/JP271573.

[33] Z. Qu, L.-H. Xie, R. Olcese, H. S. Karagueuzian, P.-S. Chen, A. Garfinkel, and J. N. Weiss, *Early afterdepolarizations in cardiac myocytes: Beyond reduced repolarization reserve*, Cardiovasc. Res., 99 (2013), pp. 6–15, https://doi.org/10.1093/cvr/cvt104.

[34] D. Sato, C. E. Clancy, and D. M. Bers, *Dynamics of sodium current mediated early afterdepolarizations*, Heliyon, 3 (2017), e00388, https://doi.org/10.1016/j.heliyon.2017.e00388.

[35] D. Sato, L.-H. Xie, T. P. Nguyen, J. N. Weiss, and Z. Qu, *Irregularly appearing early afterdepolarizations in cardiac myocytes: Random fluctuations or dynamical chaos?*, Biophys. J., 99 (2010), pp. 765–773, https://doi.org/10.1016/J.BPJ.2010.05.019.

[36] D. Sato, L.-H. Xie, A. A. Sovari, D. X. Tran, N. Morita, F. Xie, H. Karagueuzian, A. Garfinkel, J. N. Weiss, Z. Qu, and H. L. Swinney, *Synchronization of chaotic early afterdepolarizations in the genesis of cardiac arrhythmias*, Proc. Natl. Acad. Sci. USA, 106 (2009), pp. 2983–2988, https://doi.org/10.1073/pnas.0809148106.

[37] Y. Song, J. C. Shryock, and L. Belardinelli, *An increase of late sodium current induces delayed afterdepolarizations and sustained triggered activity in atrial myocytes*, Amer. J. Physiol., 294 (2008), pp. H2031–H2039, https://doi.org/10.1152/ajpheart.01357.2007.

[38] Y. Song, J. C. Shryock, S. Wagner, L. S. Maier, and L. Belardinelli, *Blocking late sodium current reduces hydrogen peroxide-induced arrhythmogenic activity and contractile dysfunction*, J. Pharmacol. Exp. Therapeutics, 318 (2006), pp. 214–222, https://doi.org/10.1124/jpet.106.101832.

[39] Z. Song, C. Y. Ko, M. Nivala, J. N. Weiss, and Z. Qu, *Calcium-voltage coupling in the genesis of early and delayed afterdepolarizations in cardiac myocytes*, Biophys. J., 108 (2015), pp. 1908–1921, https://doi.org/10.1016/j.bpj.2015.03.011.

[40] C. I. Spencer and J. S. K. Sham, *Effects of $Na^+/Ca^{2+}$ exchange induced by SR $Ca^{2+}$ release on action potentials and afterdepolarizations in guinea pig ventricular myocytes*, Amer. J. Physiol., 285 (2003), pp. H2552–H2562, https://doi.org/10.1152/ajpheart.00274.2003.

[41] S. S. Stojilkovic, J. Tabak, and R. Bertram, *Ion channels and signaling in the pituitary gland*, Endocr. Rev., 31 (2010), pp. 845–915, https://doi.org/10.1210/er.2010-0005.

[42] P. Szmolyan and M. Wechselberger, *Canards in $\mathbb{R}^3$*, J. Differential Equations, 177 (2001), pp. 419–453, https://doi.org/10.1006/jdeq.2001.4001.

[43] D. X. Tran, D. Sato, A. Yochelis, J. N. Weiss, A. Garfinkel, and Z. Qu, *Bifurcation and chaos in a model of cardiac early afterdepolarizations*, Phys. Rev. Lett., 102 (2009), 258103, https://doi.org/10.1103/PhysRevLett.102.258103.

[44] G. Tse, *Mechanisms of cardiac arrhythmias*, J. Arrhythmia, 32 (2016), pp. 75–81, 052205, https://doi.org/10.1016/j.joa.2015.11.003.

[45] T. Vo and R. Bertram, *Why pacing frequency affects the production of early afterdepolarizations in cardiomyocytes: An explanation revealed by slow-fast analysis of a minimal model*, Phys. Rev. E (3), 99 (2019), 052205, https://doi.org/10.1103/PhysRevE.99.052205.

[46] T. Vo, R. Bertram, and M. Wechselberger, *Bifurcations of canard-induced mixed mode oscillations in a pituitary lactotroph model*, Discrete Cont. Dyn. Syst. Ser. A, 32 (2012), pp. 2879–2912, https://doi.org/10.3934/dcds.2012.32.2879.

[47] M. Wechselberger, *Existence and bifurcation of canards in $\mathbb{R}^3$ in the case of a folded node*, SIAM J. Appl. Dyn. Syst., 4 (2005), pp. 101–139, https://doi.org/10.1137/030601995.

[48] J. N. Weiss, A. Garfinkel, H. S. Karagueuzian, P.-S. Chen, and Z. Qu, *Early afterdepolarizations and cardiac arrhythmias*, Heart Rhythm, 7 (2010), pp. 1891–1899, https://doi.org/10.1016/j.hrthm.2010.09.017.

[49] J. N. Weiss, Z. Qu, and K. Shivkumar, *Electrophysiology of hypokalemia and hyperkalemia*, Circ. Arrhythm. Electrophysiol., 10 (2017), https://doi.org/10.1161/CIRCEP.116.004667.

[50] D. Wilson, B. Ermentrout, J. Němec, and G. Salama, *A model of cardiac ryanodine receptor gating predicts experimental $Ca^{2+}$-dynamics and $Ca^{2+}$-triggered arrhythmia in the long QT syndrome*, Chaos, 27 (2017), 093940, https://doi.org/10.1063/1.5000711.

[51] L.-H. Xie, F. Chen, H. S. Karagueuzian, and J. N. Weiss, *Oxidative-stress-induced afterdepolarizations and calmodulin kinase* II *signaling*, Circ. Res., 104 (2009), pp. 79–86, https://doi.org/10.1161/CIRCRESAHA.108.183475.

[52] Y. Xie, Z. Liao, E. Grandi, Y. Shiferaw, and D. M. Bers, *Slow $[Na]_i$ changes and positive feedback between membrane potential and $[Ca]_i$ underlie intermittent early afterdepolarizations and arrhythmias*, Circ. Arrhythm. Electrophysiol., 8 (2015), pp. 1472–1480, https://doi.org/10.1161/CIRCEP.115.003085.